THE RESPONSE OF IONOSPHERE AND THERMOSPHERE TO THE HIGH LATITUDE ENERGY DEPOSITION

by

Yang Lu

DISSERTATION

Submitted in partial fulfillment of the requirements
for the degree of Ph.D of Science in physics at
The University at Texas at Arlington
December 2018

Arlington, Texas

Supervising Committee:

Yue Deng, Supervising Professor
Qiming Zhang
Sangwook Park
Ramon Lopez
Manfred Cuntz

ACKNOWLEDGEMENTS

I would like to thank my advisor, Dr. Yue Deng, for her help with the research that I have done, both for her guidance of this project and for the amount of time that she has spent explaining and teaching me the concepts used in this work. In addition, thanks to Dr. Cheng Sheng and Dr. Cissi Lin for reviewing the work presented here and their kind help with GITM used in the work. A special thank you to Dr. Xinan Yue who provided access to the electron density profile data from COSMIC satellites used in this analysis. Additionally, I would like to acknowledge APL/JHU web for the use of DMSP polar cap boundary data. I could not have done this without help from and discussion with those in High Latitude Observatory, Dr.Delores Knipp and Dr. Liam Kilcommons. They calculated the Poynting flux from DMSP F15 data and helped me understand those methods.

Dedication

To my family, for their continual support and encouragement to persevere through the difficult times, and for their love and caring that have uplifted me time.

ABSTRACT

THE RESPONSE OF IONOSPHERE AND THERMOSPHERE TO THE HIGH LATITUDE ENERGY DEPOSITION

Yang Lu, Ph.D.

The University of Texas at Arlington, 2018

Supervising Professor: Yue Deng

The ionosphere and thermosphere are the important regions in the Earth upper atmosphere. They represent the ionized and neutral particles, respectively. The main external energy sources in those regions are solar radiation and geomagnetic energy due to the solar wind-magnetosphere interaction. The neutral particles are ionized by solar radiation on the dayside. Meanwhile, the energy deposition from the magnetosphere is also critical at high latitudes.

The energy source at high latitudes depends on whether the local magnetic field line is closed or not. In the polar cap region where it is connected to open magnetic field line, the main energy source is from solar wind or the magnetosheath. In the aurora region where it is related to the closed field line, the main energy source is from magnetotail. The Poynting flux and particle precipitation are two kinds of energy sources at high latitudes. Energy deposition at high latitudes influences the ionization and electrodynamics in the upper atmosphere, which has practical importance since the ionization particles in the upper atmosphere influence the radio propagation

significantly. Therefore, the high latitude ionosphere and thermosphere are the most dynamic regions in the upper atmosphere since the different kinds of energy deposition.

In this work, the energy deposition and the ionosphere/thermosphere response at the high latitudes have been studied. First, Constellation Observing System for Meteorology, Ionosphere, and Climate (COSMIC) electron density profiles are used to study the conductance at different altitudes. Ionospheric conductivity plays an important role in the magnetosphere-ionosphere coupling. The altitudinal distribution of Pedersen conductivity gives us a rough idea about the altitudinal distribution of Joule heating at high latitudes, which is of great significance regarding the response of upper atmosphere to geomagnetic energy inputs. Based on the electron density profiles derived from the COSMIC measurements during 2009–2014, Pedersen conductivity has been estimated. A climatologic study of the height-integrated Pedersen conductivity in

both E (100–150 km) and F (150–600 km) regions, and their ratio under different solar and geomagnetic conditions has been conducted.

Second, the Poynting flux and particle precipitation data from DMSP F15 are used to study the energy deposition in the polar cap boundary regions. Poynting flux, which describes electromagnetic energy flux, is an important energy source for the high-latitude upper atmosphere. After the launch of Defense Meteorological Satellite Program (DMSP) F15 spacecraft with a boom-mounted magnetometer on board, there was a new opportunity to calculate Earth-directed Poynting flux at satellite altitudes (~850 km) in the upper atmosphere. A persistent enhancement of thermospheric

density in the dayside polar cap boundary regions has been reported in the CHAMP satellite observations. To understand the significance of different physical mechanisms including Poynting flux and particle precipitation, and the correlation between them, a statistical study of Poytning flux and particle energy flux in the dayside cusp and low-latitude boundary layer (LLBL) regions has been conducted based on DMSP F15 measurements.

At last, the Global Ionosphere and Thermosphere Model (GITM) are used to study the response to the geomagnetic storm event. Ion velocity in the Sub Aurora region observed by Satellites in storm time often shows a significant westward component. The high-speed westward stream is distinguished with convection pattern. This kind of events is called Sub Aurora Polarization Stream (SAPS). In March 17th 2013 storm, DMSP F18 satellite observed several SAPS cases when crossing Sub Aurora region. In this study, Global Ionosphere Thermosphere Model (GITM) has been coupled to UCLA-RCM model to simulate the impact of SAPS during March 2013 event on the ionosphere/ thermosphere.

TABLE OF CONTENTS

ACKNOWLEDGEMENTS..... i

DEDICATION.....ii

ABSTRACT.....iii

LIST OF FIGURES.....iv

LIST OF TABLES.....v

CHAPTER ONE: INTRODUCTION.....13

1.1 The solar wind.....13

1.2 The magnetosphere.....15

1.3 The ionosphere.....19

1.4 Magnetosphere-Ionosphere coupling.....22

CHAPTER TWO: PEDERSEN CONDUCTIVITY AND JOULE HEATING IN THE UPPER ATMOSPHERE.....24

2.1 Introduction to Pedersen conductivity and Joule heating.....24

2.2 Data source and methodology.....26

2.3 Pedersen conductivity dependence on Ap.....28

2.4 Pedersen conductivity dependence on F107.....35

2.5 Discussion and Summary.....41

CHAPTER THREE: POYNTING FLUX IN THE DAYSIDE POLAR CAP BOUNDARY REGIONS....43

3.1 Introduction of polar cap boundary regions.....43

3.2 Data source and methodology.....45

3.3 Results.....49

3.4 Summary and Discussion.....58

CHAPTER FOUR: GITM SIMULATION OF SAPS EVENT IN GEOMAGNETIC STORM.....60

4.1 Introduction of GITM.....60

4.2 Introduction of the SAPS event.....61

4.3 DMSP observation.....63

4.4 Eelctrodynamic forcing from RCM 67

4.5 GITM simulation results 70

4.6 Discussion.....81

CHAPTER FIVE: CONCLUSION AND FUTURE WORK.....83

REFERENCES.....86

LIST OF FIGURES

1.1 The solar wind, Sun structure and Earth……..……14

1.2 Plasma regions and current systems in the magnetosphere ……17

1.3 Duskside view of Dungey Cylcle ……..……19

1.4 Altitude profiles of temperature and number density in the atmosphere……20

1.5 demonstrating how field-aligned currents and electric fields ……..23

2.0 The conductivity profile in the ionosphere ……25

2.1 demonstrating how COSMIC using tangent point for occultation ……28

2.2 The Ap and F10.7 indices during the year 2009-2015……..29

2.3 Pedersen conductivity in the northern hemisphere in different Ap……30

2.4 Pedersen conductivity in the southern hemisphere in different Ap……33

2.5 Comparisons of $_{\Sigma PE}$, Σ_{PF}, and their ratio (Σ_{PE}/Σ_{PF}) between the two hemispheres at MLT =21–22 and MLT = 02–03 under different geomagnetic conditions……34

2.6 Pedersen conductivity in the northern hemisphere in different F10.7……36

2.7 Pedersen conductivity in the southern hemisphere in different F10.7……..39

2.8 Comparisons of $_{\Sigma PE}$, Σ_{PF}, and their ratio (Σ_{PE}/Σ_{PF}) between the two hemispheres at MLT =21–22 and MLT = 02–03 under different solar activity conditions……40

3.1 The schematic show for the cusp and LLBL……..44

3.2 DMSP F15 observations on 5 Jun, 2000……..49

3.3 DMSP F15 observations on 27 July, 2002……50

3.4 The number comparison between the cusp and LLBL in each category……52

3.5 Correlation between IMF conditions and the maximum Poynting flux……..54

3.6: The correlation between Poynting flux and electron precipitation energy flux……..57

4.1: The DMSP observation from 1650UT to 1730UT March 17th 2013……65

4.2 The ion drift observation from DMSP F18 March 17th 2013……66

4.3 The whole forcing pattern to GITM March 17th 2013……..67

4.4 The electron energy flux from RCM output at March 17th 2013……69

4.5 The potential pattern from RCM output at March 17th 2013……70

4.6 Dst index during March 17-18, 2013……71

4.7 The GITM simulation results of neutral wind and ion drift from DMSP drive March 17th 2013……73

4.8 The GITM simulation results force terms along the DMSP track March 17th 2013…..75

4.9 The GITM simulation results of ion drift from RCM drive March 17th 2013……..77

4.10 The GITM simulation results of neutral wind from RCM drive March 17th 2013……77

4.11 The GITM simulation results of ion drift at the LT 18 from RCM drive March 17th 2013……78

4.12 The GITM simulation results of Pedersen conductance at the LT 18 from RCM drive March 17th 2013……..80

4.13 The DMSP observation from f16 of ion drift March 17th 2013……..81

CHAPTER 1

Introduction

The upper atmosphere is one part of near-earth space environment system at 100 – 600 km altitudes, which includes both ionosphere and thermosphere. The ionosphere is the ionized part and the thermosphere is the neutral parts. The upper atmosphere is not an independent system. The external energy sources include the solar radiation, solar wind, magnetosphere, lower atmosphere and so on. They are highly dynamic and tightly coupled with each other as an interactive system. In the introduction part, the whole picture of the near-earth space system and how they influence each other are discussed.

1.1 The solar wind

The Sun is the closest star to the Earth and it is the main energy source for our Earth environment system. The solar radiation, which is the electromagnetic energy, has been studied since a very early time. However, people realized the existence of flowing outward particles from the Sun until 20th century. Therefore, the space between Earth and the Sun is not a vacuum. The Earth system is surrounded by the ionized particles from the Sun, which is also known as solar wind nowadays. Scientists suggested the existences of these outflow particles from the Sun throughout the observations of solar corona and comet tail. People could measure the solar wind in situ only after the launch of the first spacecraft.

The solar wind is a supersonic flow away from the Sun in all directions but not uniform

[*Parker,* 1958]. The origin of the solar wind is solar corona and the typical velocity of solar wind varies from 250 km/s to 750km/s [*Brandt*, 1973]. The speed of solar wind depends on the origin region of solar wind on the Sun. Usually, the solar wind coming from corona holes tends to have higher speed. The solar wind plasma is quasi-neutral and the density is commonly few protons /cm^3 [*Parker,* 1958]. Since the density in the solar wind plasma is very small, it is considered as collisionless plasma. Not only the solar wind carries the kinetic energy from the Sun, it also carries the magnetic field from the Sun, which is known as interplanetary magnetic field (IMF) [*Parker,* 1963]. The magnetic field lines move along with solar wind plasmas, which is named as the magnetic-frozen [*Alfvén,* 1942]. Most recently, the NASA's Parker Solar Probe was launched in 2018 summer to dedicate to the measurements of the solar wind in situ.

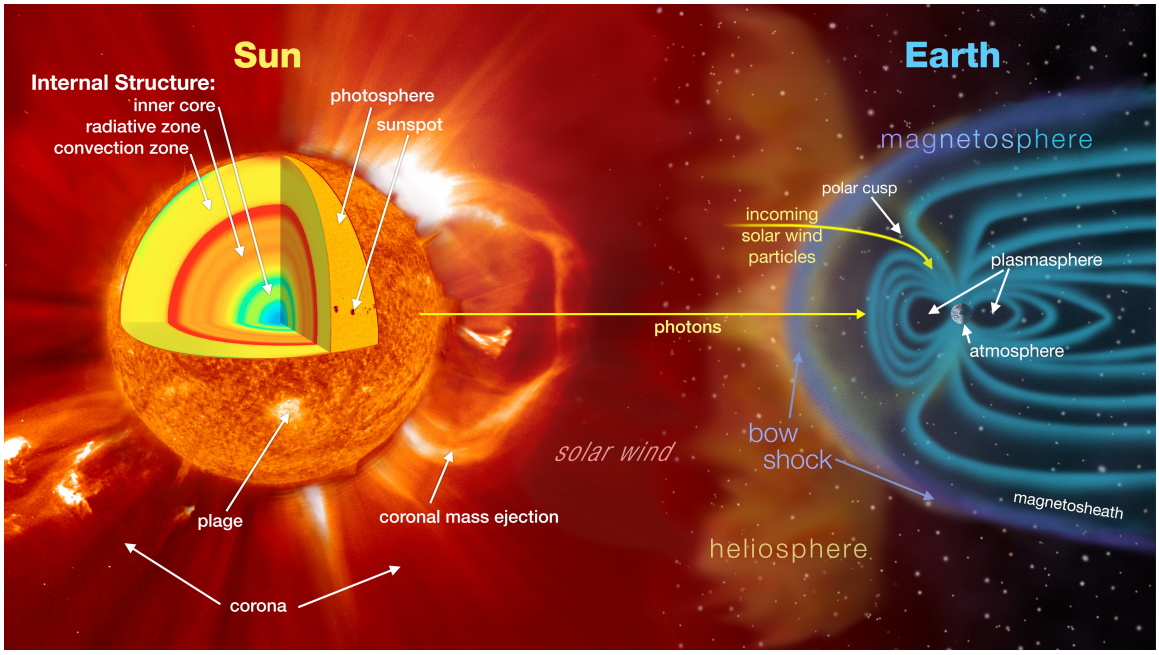

Figure 1.1: A cartoon showing the Sun structure, solar wind and the Earth's magnetosphere. (Courtesy of NASA)

1.2 The magnetosphere

The Earth magnetosphere is a dipole field created by hot iron and nickel cores. Many charged particles are trapped in the magnetosphere. The Earth magnetosphere is reshaped due to the solar wind dynamic pressure. The dayside is compressed around 10~ 12Re and the night-side is stretched to over 100 Re. The Earth magnetosphere in the solar wind is like an obstacle in the stream. It shields Earth from the direct influence of solar wind. The magnetopause is the boundary of Earth's magnetic field and solar wind field. The position is the balance between the solar wind dynamic pressure and Earth magnetic pressure. As shown in Figure 1.2, the solar wind flow will be deflected when reach the magnetopause. There exists the discontinuity of magnetic field between the outside magnetopause and inside magnetopause, so current system must exist to maintain the discontinuity. Therefore, the magnetopause is a current sheet in the space. [Kivelson and Russell, 1995]. Based on the characteristics of the plasma, the magnetopause is divided into three different types of boundary layers: the High Latitude Boundary Layer (HLBL), the Low Latitude Boundary Layer (LLBL), and the cusp (entry region) [Kivelson and Russell, 1995]. Those boundary regions will have different influence on the Earth upper atmosphere. Inside the magnetopause is the region which we call the magnetosphere. The magnetosphere is also divided into the inner magnetosphere and the outer magnetosphere.

The night-side outer magnetosphere has two lobe regions and a plasma sheet. At the lower latitude region is the plasma sheet. The plasma sheet consists of hot plasma and

the density is much higher than the two lobe regions. At the higher latitude, are the two lobe regions: the northern lobe and the southern lobe [Kivelson and Russell, 1995]. The magnetic field in these two regions are opposite directions. At the northern lobe, the magnetic field line is towards the Earth while at the southern lobe region, the magnetic field line is anti-towards the Earth. The inner magnetosphere shape is close to the dipole field. The inner magnetosphere is divided into the radiation belts and the plasmasphere based on the properties of plasma. The radiation belt is also called the Van Allen radiation belt, since it is discovered and confirmed by the Van Allen at the University of lowa based on the Explorer 1 and Explorer3 in early 1958. The radiation belts consist of energetic particles trapped by the Earth's magnetic field. Energies vary from a few keV to MeV [Schunk and Nagy, 2009]. There exist two belts, the inner belt and the outer belt. The inner belt consists of trapped high energy ions and the outer belt consists of trapped high energy electrons. Typically, the range of the inner belt varies from 1 to 3 R_E and the outer belt varies from 3 to 6 R_E [Kivelson and Russell, 1995]. Compared to the radiation belts, the plasmasphere is the region consists of dense low energy plasma. It is co-located in the same region as the radiation belts. It is like a cold background compared with the hot plasma in the radiation belts. The particle energies in the plasmasphere often of 1 eV [Kivelson and Russell, 1995; Schunk and Nagy, 2009]. The plasma in the inner magnetosphere will have influence on the upper atmosphere. Some particles from ionosphere will also escape to the plasmasphere as well.

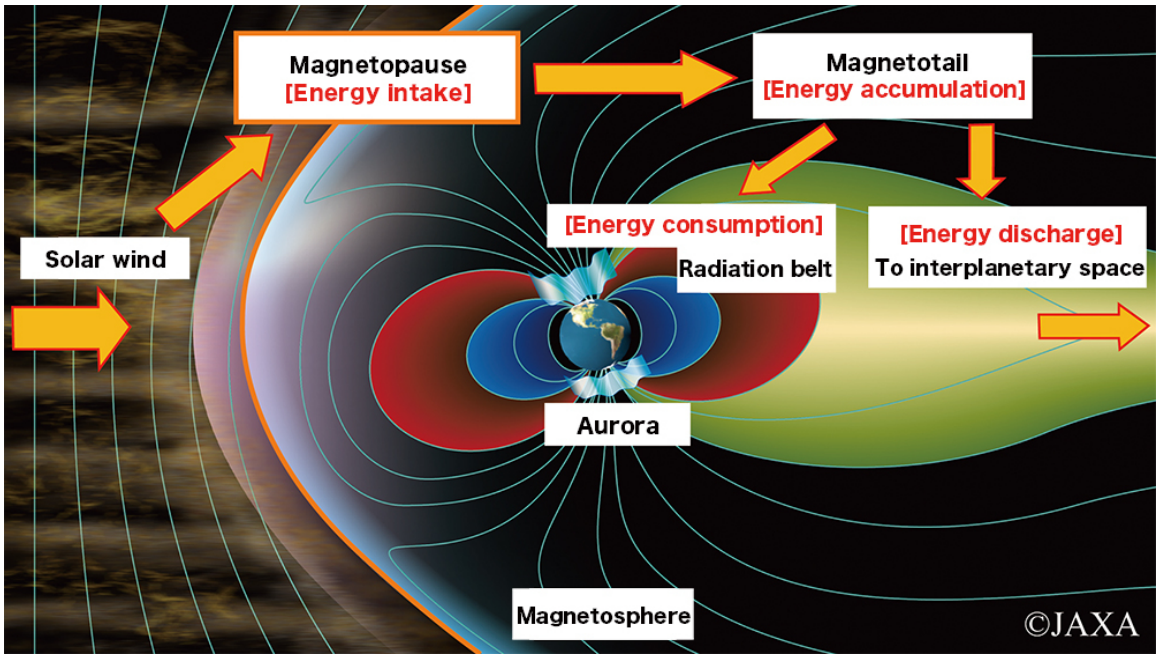

Figure 1.2: Plasma regions and current systems in the magnetosphere. See text for details. Courtesy of NASA.

As mentioned before, the solar wind flow could not penetrate the magnetopause in most cases. There has some physics process to transfer the kinetic energy from solar wind to Earth magnetosphere. Typically, the important processes in the solar wind and magnetosphere interaction is called the Dungey Cycle [Dungey, 1961]. Dungey Cycle plays an important role in the energy transfer from the solar wind to the magnetosphere. Dungey [1961] proposed the magnetic reconnection will drive the convection in the whole magnetosphere. The magnetic reconnection will happen at both the dayside and the magnetotail. Magnetic reconnection happens when the oppositely direction of magnetic field lines merge with each other and form the new field lines. It will change the topology of magnetic field. The magnetic reconnection is most likely to occur when the B_Z component of IMF is southwards, since the Earth

magnetic field lines are northward in the dayside. As it is shown in Figure 1.3, when the solar wind moves towards the Earth, it will carry the southward magnetic field moving towards Earth as well (frozen in condition). In the dayside, the southward IMF will meet the northward Earth magnetic field. Those field lines will break and merge with each other. This process will break the frozen in condition. As the solar wind moves past the Earth, it will pull the newly formed field lines anti-sunwards. Finally, the pulled field lines will merge and reconnection happen again in the magnetotail due to the magnetic pressure. As the magnetic reconnection happens in the magnetotail, part of energy carried by plasma will move towards the Earth and part of plasma will move towards the tail. The whole process will transfer the energy from solar wind particles to the Earth inner magnetosphere. This is called the Dungey Cycle. The Dungey Cycle is an important process drive the convection in the magnetosphere.

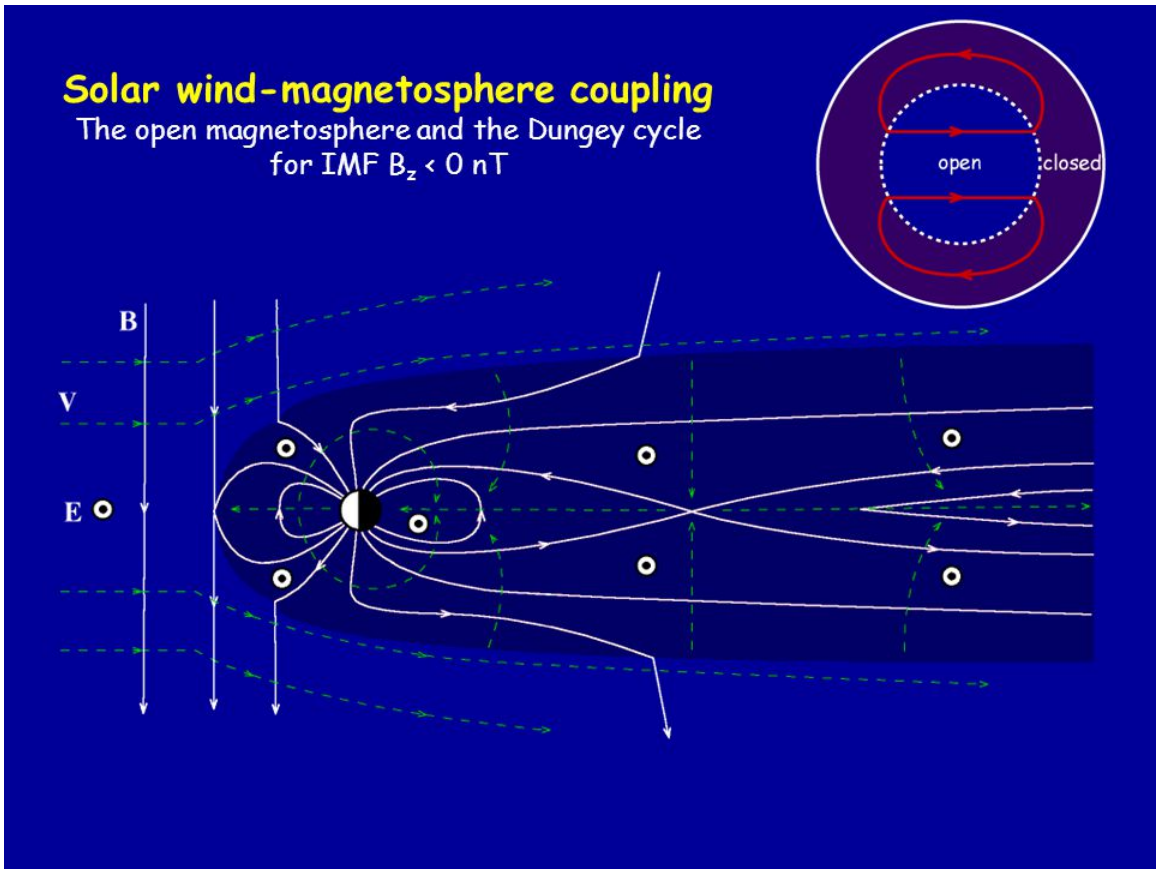

Figure 1.3: Duskside view of Dungey Cylcle. Courtesy of NASA.

1.3 The ionosphere

The ionosphere is the ionized part of the Earth's upper atmosphere. The altitudes vary from 60 to 600 km typically [Kivelson and Russell, 1995]. At the upper atmosphere, it is weakly ionized (around 1%). The ionosphere represents the ionized part and the thermosphere represents the neutral parts. Although the density of ions and electrons are much smaller than the neutral particles, the ionized plasma will play important roles. It is important to study the physics process in the ionosphere and the ionosphere-thermosphere coupling. The Figure 1.4 shows a temperature profile and density profile of the Earth's atmosphere. For neutral particles, from the bottom to the top are

Troposphere, Stratosphere, Mesosphere and the Thermosphere. As it is shown, the temperature varies a lot from solar minimum to the solar maximum. The middle part shows the penetration depth. Different wavelength of radiation will be absorbed at different altitudes. The two main energy sources of the ionization are photoionization caused by EUV and UV radiation from the solar irradiance and energetic particle precipitation [Kivelson and Russell, 1995]. Photoionization is the dominant source in the dayside ionosphere while particle precipitation is more important at high latitudes, especially the aurora region.

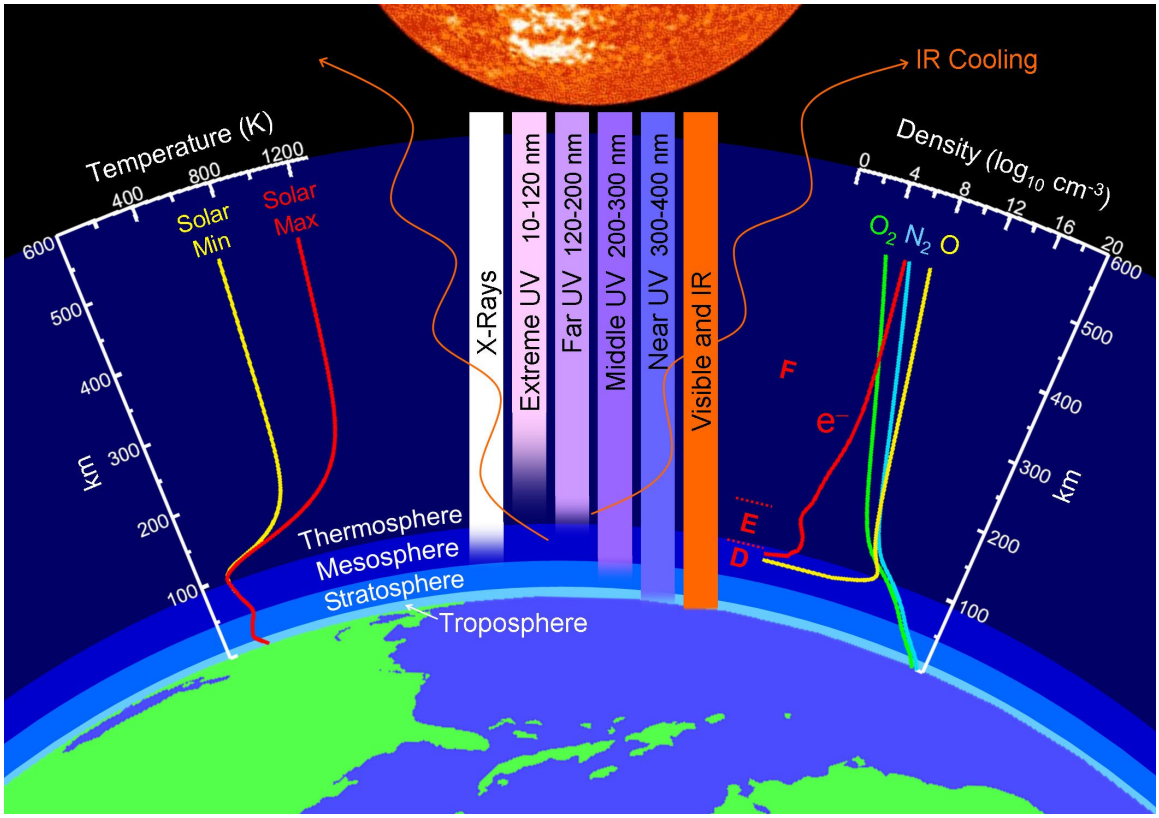

Figure 1.4: Altitude profiles of temperature and number density in the atmosphere (Courtesy of John Emmert/NRL).

As the right part in the Figure 1.4 shows, the ionosphere is divided into three regions. The D region which is the lowest region varies from 60 to 90 km. D region only appears at the dayside in most cases, because the recombination rate is high in the D region. The region between 90 to 150 km is the E region and above 150 km is the F region. The Figure 1.4 shows the electron density peak in the E region and F region clearly. Usually, the F region has the maximum plasma density in the ionosphere, it can be divide into F1 and F2 region sometimes. The formation of D region is due to the ionization of NO. The main ion species in the D region include NO^+ and O_2^+ and the neutral species include NO, O_2, N_2 [Schunk and Nagy, 2009]. The main ion species in the E region are NO^+, O_2^+ and N_2^+ while O^+ is the dominant ion species in the F region.

There are numerous physics and chemical processes in the ionosphere, including the chemical kinetics, fluid mechanics, atomic theory and plasma physics. The ionization due to EUV/UV radiation and particle precipitation determines the sources of electron. The chemical processes will determine the loss. The fluid mechanics determines the transportation process [Kivelson and Russell, 1995]. All those processes are important to understanding the ionosphere. Too much details could not be discussed here. However, it is obviously the ionosphere is not an independent system. All the external energy sources from the Sun and the magnetosphere have great impact on the ionosphere. The neutral particles and ionized particles will also influence each other. They are tightly coupled systems. In the following chapter, it will discuss the Magnetosphere-Ionosphere coupling physics.

1.4 Magnetosphere-Ionosphere coupling

The ionosphere and the magnetosphere are tightly coupled systems. The most important physics process connecting the ionosphere and magnetosphere is the field-aligned currents (FAC). The FAC is also called the Birkeland current. Figure 1.5 shows the major current systems of M-I coupling, the Region-1 and Region-2 field-aligned current (FAC) systems. The Region-1 currents flow into the ionosphere on the dawnside and flow out on the duskside. In opposite, the Region-2 currents flow into the ionosphere on the duskside while flow out on the dawnside. The Pedersen currents which are parallel to the electric field will closure the current system between the Region-1 and Region-2 in the ionosphere.

Another physics process of M-I coupling is the particle precipitation. There are many charged particles in the magnetosphere. These charged particles will bounce back and force along the magnetic field line. The bounce back point is called the magnetic mirror. If the energy of charged particles is higher, the magnetic mirror point will be at the lower altitude. It is high likely that the charged particles will collision with the neutral backgrounds when the energy is high. These energetic particles precipitation will cause ionization and excitation. As consequence, the excitation particles will emit light of varies colors. This is called the aurora. The aurora is a typical physics process caused by the M-I coupling.

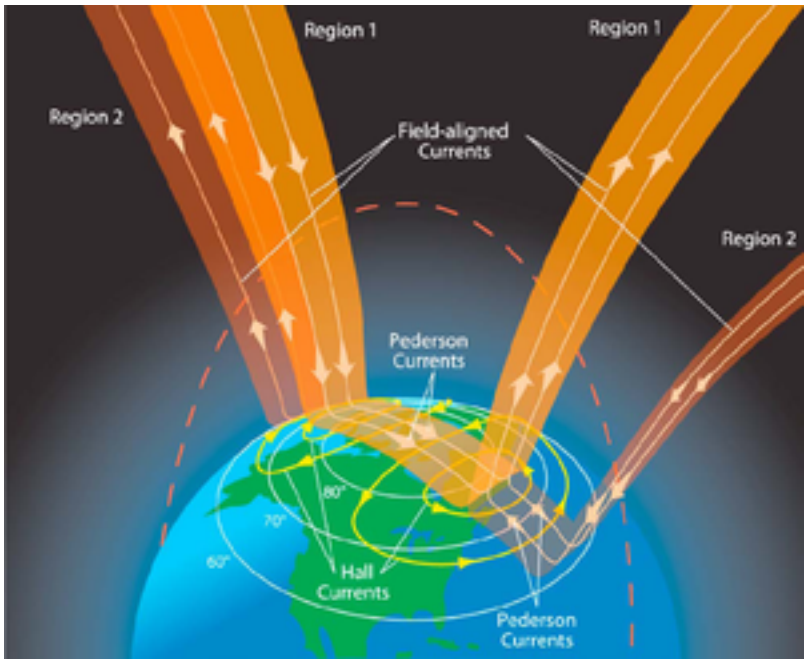

Figure 1.5: A cartoon demonstrating how field-aligned currents couple the magnetosphere and ionosphere together. [Le et al., 2010]

CHAPTER 2

PEDERSEN CONDUCTIVITY AND JOULE HEATING IN THE UPPER ATMOSPHERE

2.1 Introduction to Pedersen conductivity and Joule heating

In this chapter, the Pedersen conductivity and Joule heating in the ionosphere have been calculated. Joule heating is the energy dissipation through the current transportation. In general, the Joule heating, $\mathbf{J} = \sigma \mathbf{E}^2$, where **J** is the Joule heating in certain volume, σ is the conductivity and **E** is the electric field. Basically, the conductivity is a tensor. In the ionosphere study, the currents flow according to the Ohm's law, but the electric conductivity is anisotropic because of the effect of the geomagnetic field, and three conductivities are defined. Those are parallel, Pedersen and Hall conductivities. Parallel conductivity is for the direction parallel to the magnetic field line and denoted as "σ_0". This is the same as that when there is no magnetic field, and much larger than Pedersen and Hall conductivities in the ionosphere. Terms of "longitudinal conductivity" and "direct conductivity" are also used. Pedersen conductivity is for the conductivity in the direction perpendicular to the magnetic field and parallel to the electric field. It is denoted as "σ_p". Hall conductivity is for conductivity in the the direction perpendicular to both the magnetic and electric fields. It is denoted as "σ_h". In the ionosphere, this conductivity is due to the drift motion of the electron (ExB drift) and maximum in the E region where only electron practically drifts to the direction of ExB.

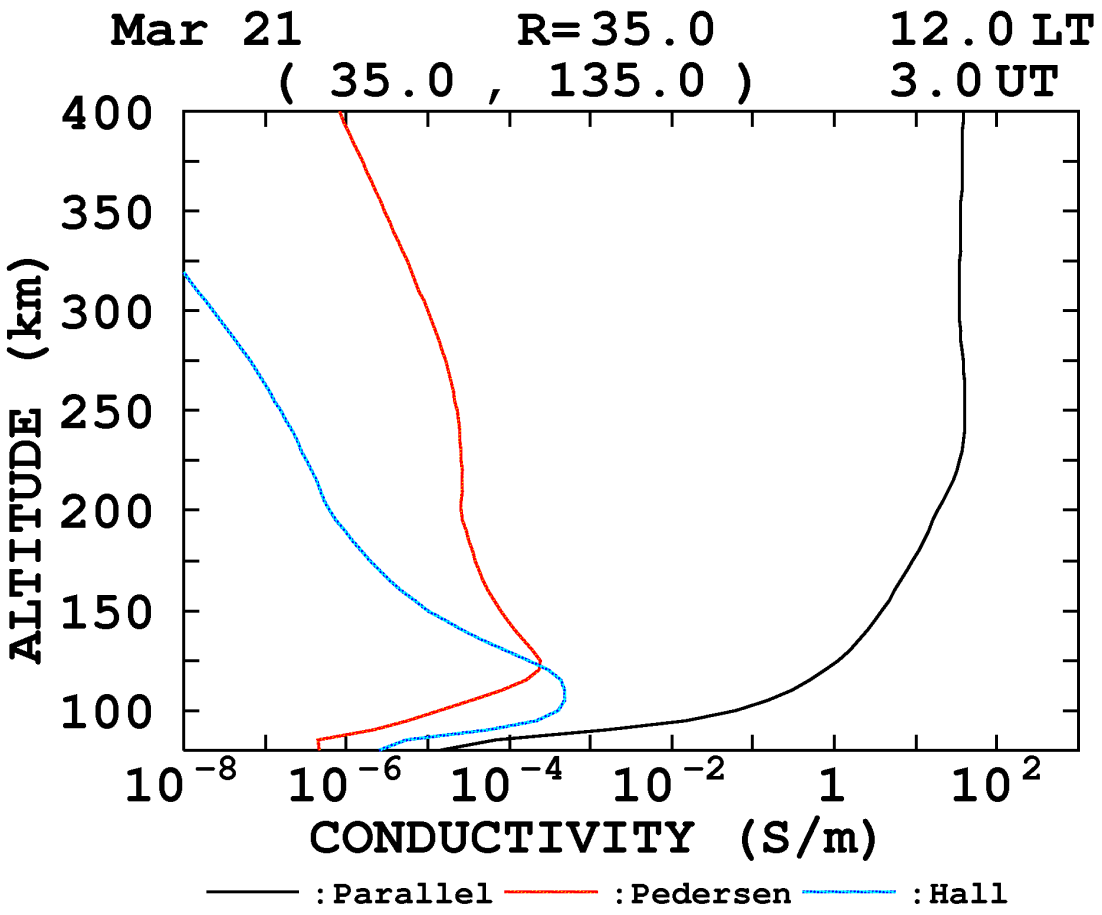

Figure 2.0: The conductivity profile in the ionosphere. Black line represents parallel conductivity. Blue line represents Hall conductivity and red line represents Pedersen conductivity. (Courtesy of WDC, Kyoto)

Figure 2.1 shows the typical conductivity profile in the ionosphere. As the figure shows, the parallel conductivity is much larger than the Pedersen conductivity and Hall conductivity in all altitudes. Below 120 km, the Hall conductivity is larger than the Pedersen conductivity while Pedersen conductivity is larger than the Hall conductivity

above 120 km.

In this study, Joule heating in the ionosphere at different altitudes is calculated through $\mathbf{J} = \sum_p \mathbf{E}^2$. In the ionosphere altitude, the **E** does not change too much along the altitude, then $\sum_p$ provides a roughly estimation of the Joule heating in the certain region. Meanwhile, $\sum_p$ determines the current system and is also an important parameter to the magnetosphere-ionosphere coupling.

In the following part of this chapter the ion profile data from COSMIC satellite will be used to calculate the $\sum_p$ in different levels of solar activities and geomagnetic activities.

2.2 Data source and methodology

In the ionosphere, the formula to calculate the Pedersen conductivity is as following.

$$\sigma_P = \frac{en_e}{B}\left\{\sum_i C_i\left[\frac{\nu_{in}/\omega_i}{1+(\nu_{in}^2/\omega_i^2)}\right] + \frac{\nu_e/\omega_e}{1+(\nu_e^2/\omega_e^2)}\right\}$$

Here σ_p is the height integrated Pedersen conductivity. B is the magnetic field strength, n_e is the electron density, e is the unit charge, C_i is the relative concentration of ion species i, ν_{in} is the collision frequency between an ion of species i and neutral particles, ω_i is the ion gyrofrequency, ν_e is the sum of electron-ion and electron-neutral collision frequencies, and ω_e is the electron gyrofrequency. In this study, those quantities will be calculated from empirical model except the electron density n_e, since the electron

density is the major contribution to the altitudinal variation of Pedersen conductivity. The ion profile data used by us in this study is from COSMIC program through 2008-2014. The COSMIC (Constellation Observing System for Meteorology, Ionosphere and Climate) is a joint mission between NSPO (National Space Program Office) of Taiwan and UCAR (University Corporation for Atmospheric Research) of the United States of America. The project launched a LEO constellation of six microsatellites. One of the purpose of the project is using the GPS signal to measure the electron density profile which will be used in this study. The method using GPS radio occultation technique is as following: When a signal travels through the atmosphere, it will be retarded and bent due to the influence by the ionosphere. The retarded and bent signal is a result in a phase and Doppler shift. This can be measured accurately through the GPS receiver aboard and the COSMIC satellites. Once the data of the transmitter and receiver positions and velocities are known from orbit information, bending angle as a function of electron density, can be computed from the Doppler shift observed at LEO. This one signal will give the information of electron density along one signal track, which is called the slant TEC. From the slant TEC, the vertical profiles can also be calculated which is called the vertical TEC. Below the figure 2.1 shows how this method is used for occultation measurements.

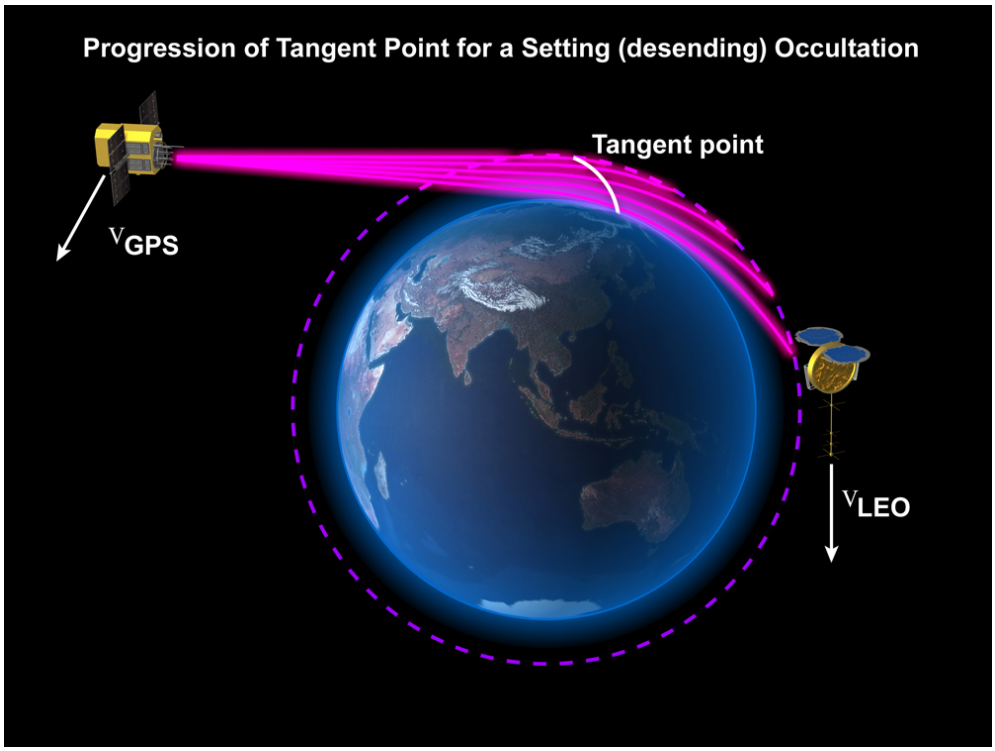

Figure 2.1: A cartoon demonstrating how COSMIC using tangent point for occultation. (Courtesy of COSMIC website)

2.3 Pedersen conductivity dependence on Ap

In this chapter, the $\sum_p$ in the ionosphere both E region and F region will be calculated during different level of solar activities and geomagnetic activities. In previous formula, it shows that the Pedersen conductivity is mainly dominant by the electron density. The electron density profile in the ionosphere is determined by the ionization rate, which the EUV radiation and particle precipitation are the main energy sources. Here we introduce two space weather indices Ap and F10.7. Ap is an index which indicates the level of geomagnetic activity and F10.7 is and index which indicates the level of solar

radiation. Since the Pedersen conductivity is highly depend on the Ap and F10.7 indices, the $\sum_p$ in the E region, F region and their ratio in different Ap and F10.7 levels are analyzed. The ratio will give us an estimation of how the Joule heating distribution at different altitudes.

Figure 2.2 shows the Ap and F10.7 indices during the year 2009-2015. To investigate the $\sum_p$ dependences on different solar radiation and geomagnetic activity level, they are divided into 3 levels respectively. If Ap > 80 it is defined as the severe activity condition If 15<Ap<80, it is defined as the moderate level. If Ap<15, it is defined as the quiet level.

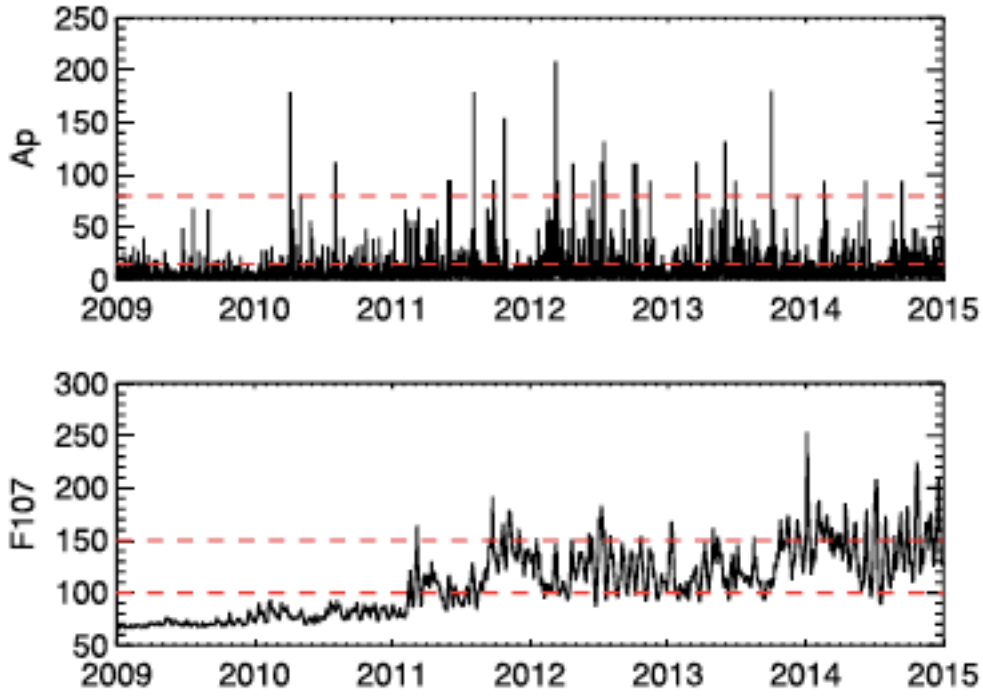

Figure 2.2: The Ap and F10.7 indices during the year 2009-2015. The red dash lines mark the level Ap =15, Ap = 80, F10.7 = 100, F10.7 =150 respectively [Sheng et al., 2017].

Similarly, for the F10.7 index, if F10.7> 150 it is defined as the severe activity condition.

If 100<F10.7<150, it is defined as the moderate level. If F10.7<100, it is defined as the quiet level. From above figure, it shows the trend of Ap and F10.7 during the year 2009-2015. In the long term trend the F10.7 increases during these years, since the F10.7 is corresponding to the solar circle. The Ap index also increases averagely, but the trend is not coincided with the F10.7.

The COSMIC electron profile data using 5x5 degree grid both latitude and longitude in different Ap and F10.7 levels will be binned. Then calculate the height integrated Pedersen conductivity in the E (100-150km) and F (150-600 km) regions.

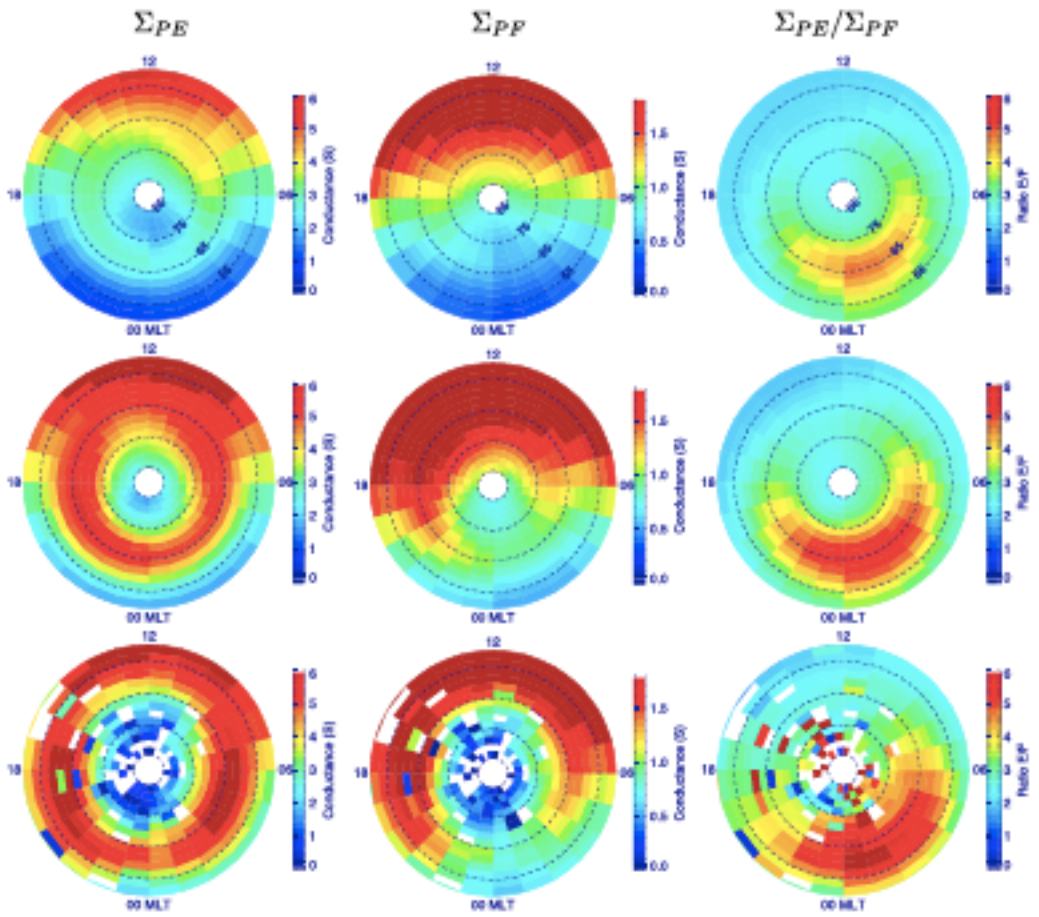

Figure 2.3 Pedersen conductivity in the E(left), F(middle) region and their ratio(right) in the northern hemisphere. From the top to the bottom rows are quiet (Ap<15), moderate(15<Ap<80) and severe (Ap>80) respectively [Sheng et al., 2017].

Figure 2.3 shows the Pedersen conductivity generated by the COSMIC electron profile in the northern hemisphere. The left column is the $\sum_{pe}$ which is the height integrated Pedersen conductivity in the E region (100-150 km). The middle column is the $\sum_{pf}$ which is the height integrated Pedersen conductivity in the F region (150-600 km) and the right column is their ratio. The top row is the quiet condition (Ap<15). The middle row is the moderate condition (15<Ap<80) and the bottom row is the severe condition (Ap>80). The Magnetic Apex coordinates are applied to the results. From previous figure 2.1, it could be known that the data for Ap> 80 is very limited, so the results of bottom row may be not as reliable as the top two rows. The results of severe condition will not be emphasized. From the figure 2.2, it could find that both $\sum_{pe}$ and $\sum_{pf}$ get maximum on the dayside for all different conditions. That means the solar radiation contribute most in the Pedersen conductivity. And the Pedersen conductivity also have localized peak near the aurora region. This is because in the aurora region the particle precipitation will have strong influence on the conductivity. The right column shows the ratio between the conductivity in the E region and F region. It could be clearly identified that in the aurora region there exists the local peak. And the ratio also increases in the moderate case compare to the quiet case. The result indicates the particle precipitation will change the Pedersen conductivity more in the E region than the F region. It could be concluded that the energy transportation from magnetosphere due to particle

precipitation will most deposit into the E region. It could also be noticed that in the moderate case, the peak value in the aurora region is increased by 2~4 S in the E region. In the F region, the conductivity also increases. This is because the intense geomagnetic activity intense the aurora particle precipitation. In the F region, the contribution is most from soft particles. Additionally, the peak value in the aurora in the E region is comparable to the dayside. That means the significant contribution of particle precipitation to the total conductivity. Furthermore, it could be noticed that in all cases, the peak value of conductivity in the pre-midnight sector is larger than in the post-midnight sector in the aurora region, however the ratio peak appears in the post-midnight sector. And the large value of ratio also expands to the lower latitude. This needs more discussion in the following paragraphs.

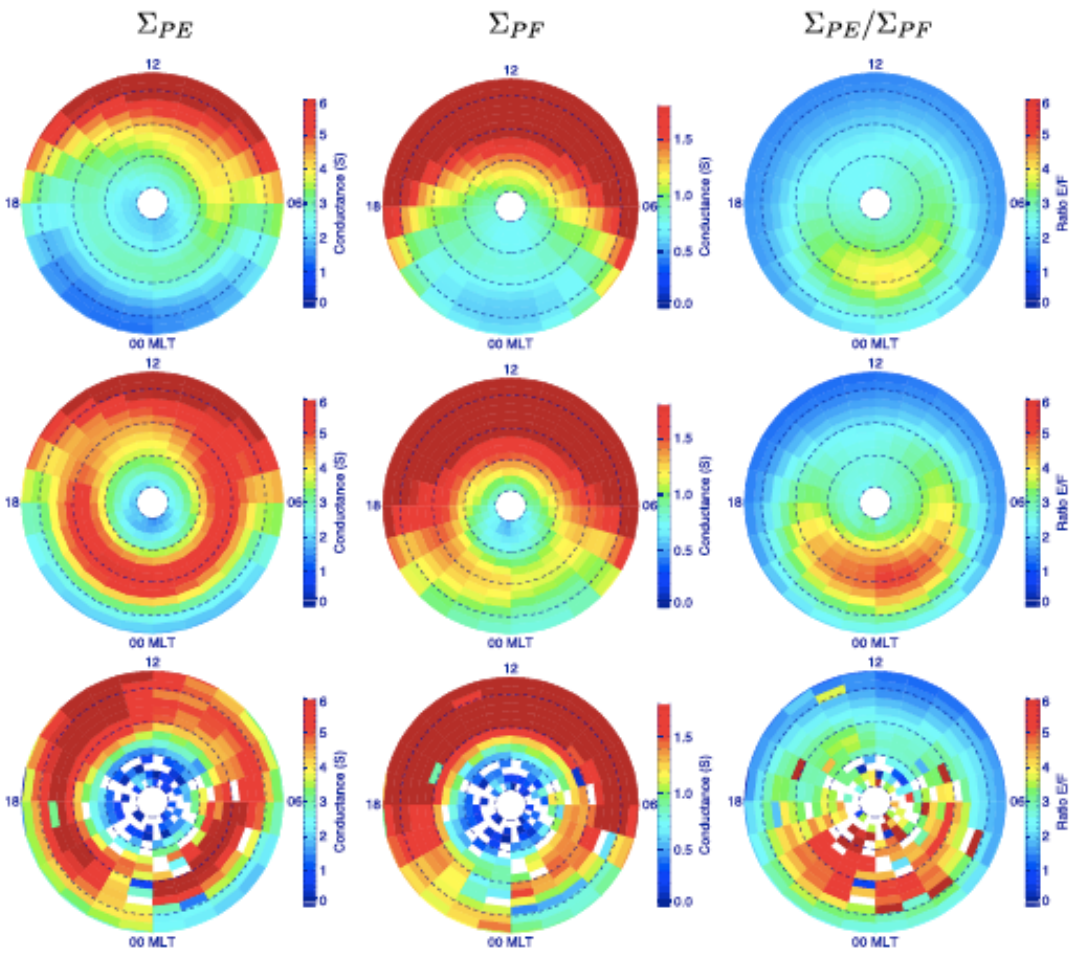

Figure 2.4 Similar to the figure 2.3, but for the southern hemisphere [Sheng et al., 2017].

Above the figure 2.4 shows the similar results in the southern hemisphere. The global feature is quite similar, but there also exits some differences to the northern hemisphere. It could be noticed that the peak value in the aurora region in the southern hemisphere is larger than in the northern hemisphere, but the peak value of ratio is lower than in the northern hemisphere. That indicates the existence of interhemispheric asymmetry. To investigate the asymmetry between the different hemisphere and local time, the maximum value of Pedersen conductivity in both E region and F region as well

as their ratio in different local time sector are extracted.

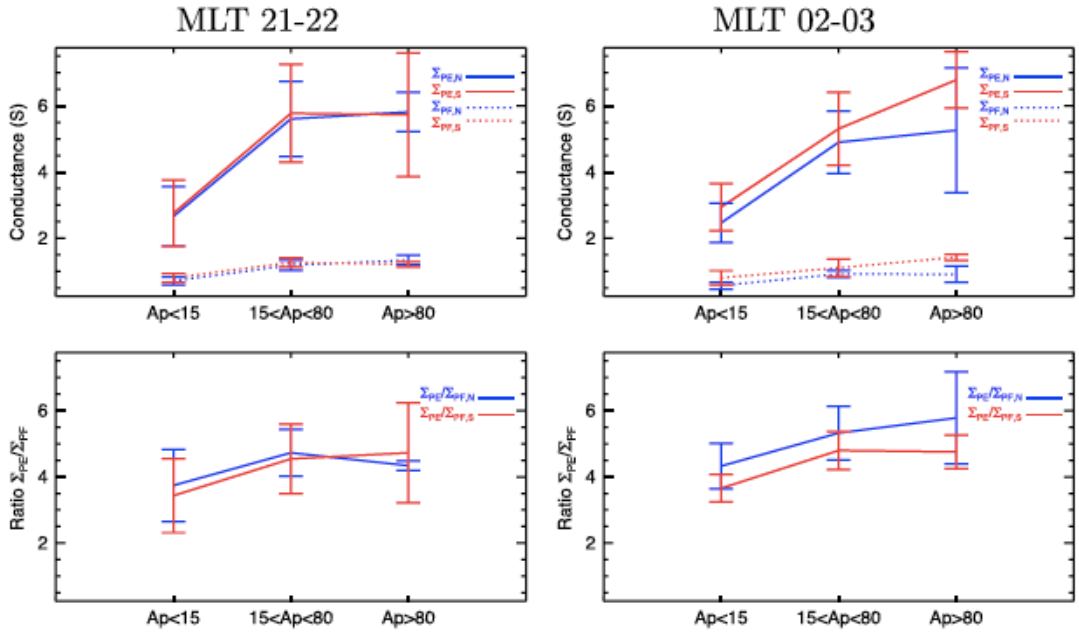

Figure 2.5. Comparisons of ΣPE, ΣPF, and their ratio (ΣPE⁄ΣPF) between the two hemispheres at (left column) MLT =21–22 and (right column) MLT = 02–03 under different geomagnetic conditions. For each local time, the location with maximum ΣPE is selected to ensure the comparisons in the aurora zone. Blue lines show for the Northern Hemisphere, and red lines show for the Southern Hemisphere. In the (top row) conductance plots, solid lines plot ΣPE and dashed lines plot ΣPF. Error bars represent standard deviation [Sheng et al., 2017].

Figure 2.5 shows Pedersen conductivity dependence of Ap index. The top row is the conductivity in the E region and F region. The bottom panel shows the ratio. The left part is the MLT 21-22 which is the pre-midnight sector and the right part is the MLT 02-23 which is the post-midnight sector. The blue line represents the northern hemisphere

and red line represents the southern hemisphere. There also exists a relative standard deviation of 10%-30% as indicated by the error bar. As it shows in the figure 2.5, in the pre-midnight sector, the difference of conductance and their ratio in different hemisphere is negligible. However, in the post-midnight sector, both Σ_{PE} and Σ_{PF} are slightly larger in the Southern Hemisphere, which may result from the unequal solar radiation in the aurora zone between the two hemispheres

due to the displacement between the geomagnetic and geographic poles. Though the conductance is larger in the northern hemisphere, the ratio in the southern hemisphere is larger than in the northern hemisphere. This indicates the local time dependence of interhemispheric asymmetry. We suspect that not only solar radiation but also auroral activity are different in the auroral zone between the two hemispheres.

Due to the limitation of available data, the solar flux effect was not separated when investigating the Ap dependency of Σ_{PE}, Σ_{PF}, and ratio. It can be seen fromFigure 1 that the Ap index was more likely to be larger than 15 from 2011 to 2015 when the F10.7 was relatively larger. As it can be calculated the average F10.7 and Ap indices for each longitude-latitude bin, the average F10.7 index rises from ~95 to ~110 at most bins when the geomagnetic condition changes from quiet (Ap<15) to moderate (15< Ap < 80). Meanwhile, the average Ap index jumps from ~4.5 to ~29. Therefore, the influence of change in solar flux should be secondary compared with that of change in geomagnetic activity.

2.4 Pedersen conductivity dependence on F10.7

In previous paragraphs, the Pedersen conductivity dependence on the Ap has been discussed. Using similar method, the dependence on F10.7 in the following paragraphs will be discussed. The F10.7 implies the intensity of solar radiation while Ap implies the geomagnetic activity level.

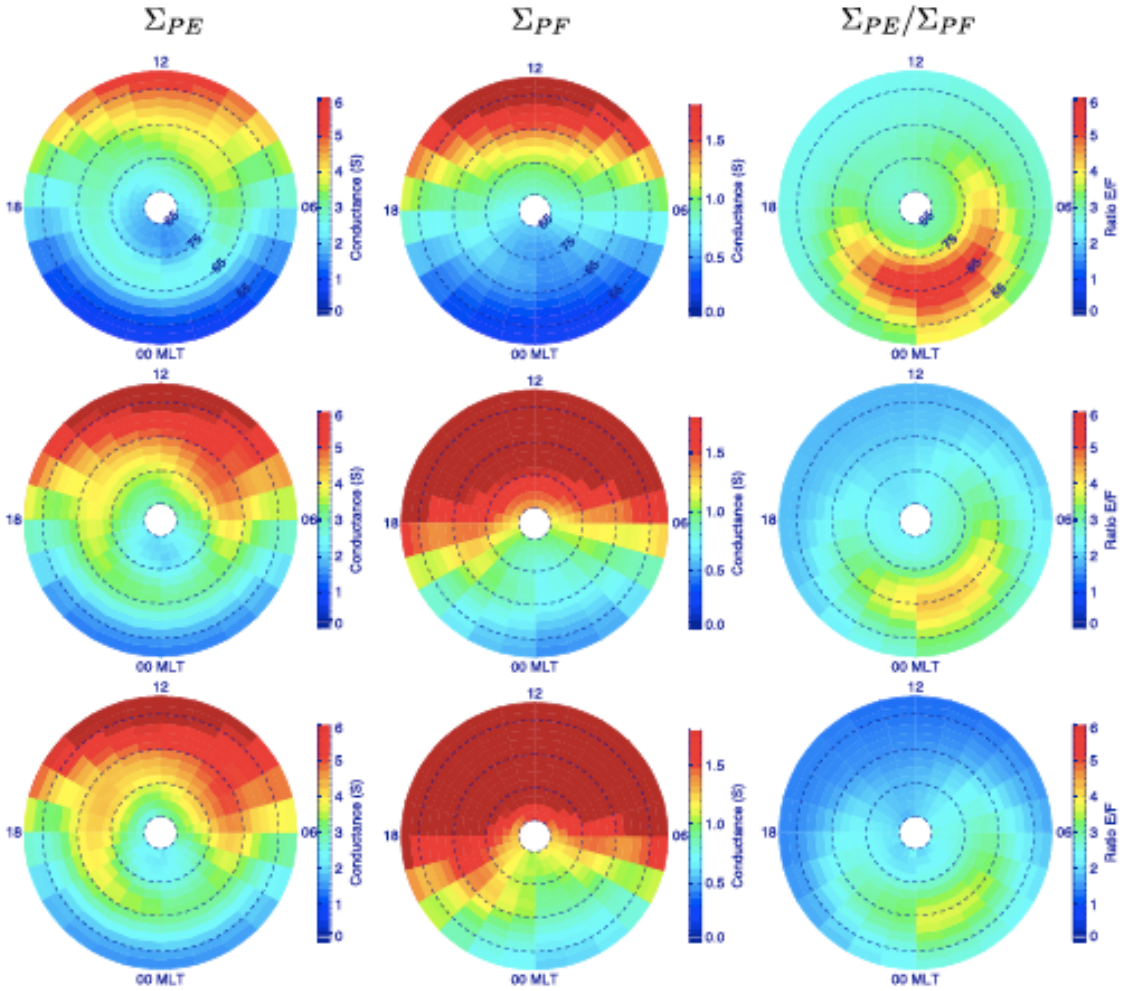

Figure 2.6 Pedersen conductivity in the E(left), F(middle) region and their ratio(right) in

the northern hemisphere. From the top to the bottom rows are quiet (F10.7<100), moderate(100<F10.7<150) and severe (F10.7>150) respectively [Sheng et al., 2017].

Above the figure 2.6 shows the height integrated Pedersen conductivity.

Similar to figure 2.3 and figure 2.4, the left column is the $\sum_{pe}$ which is the height integrated Pedersen conductivity in the E region (100-150 km). The middle column is the $\sum_{pf}$ which is the height integrated Pedersen conductivity in the F region (150-600 km) and the right column is their ratio. The top row is the quiet condition (F10.7<100). The middle row is the moderate condition (100<F10.7<150) and the bottom row is the severe condition (F10.7>150). In this case from figure 2.2, the data base have enough coverage for all different levels, so only the data under the condition (Ap<15) are used to exclude the influence of particle precipitation. As showed in the figure, when the F10.7 increases, the magnitudes of Σ_{PE} at noon and midnight at 65◦N increase from 3.9 S to 5.0 S and 2.4 S to 3.2S, respectively, and the percentage increase are close to 25% and 35%, respectively. Meanwhile, the magnitudes of Σ_{PF} increase from 1.5 S to 3.4 S and 0.4 S to 0.9 S, respectively, which are more than 100% increase. It also shows that the region with larger conductance expands to higher latitudes when solar activity is stronger.

However, when the solar activity increases, the ratio (right column) decreases in the aurora region. Clearly, it could be identified that the change at the F region is larger than at the E region especially the dayside and the high latitude. Σ_{PE} also increases, the main contribution is still the aurora particle precipitation. Though only the quiet time

data(Ap<15) are used, it is still possible for certain geomagnetic activity change. Since F10.7 contributes the change of Pedersen conductivity mainly in the F region, the ratio decreases as the F10.7 increases. It could be concluded that both the solar activity and aurora activity change the ratio. Not surprisingly, the Pedersen conductivity and the ratio show the local time dependence as well. Similarly, it will be discussed that later.

The figure 2.7 below shows the result in the southern hemisphere. Again, two hemispheres have very similar the global features. It could be noticed that as the F10.7 increases, the Pedersen conductivity increase is stronger in the southern hemisphere than in the northern hemisphere. That is beacause the magnetic south pole locates at a lower geographical latitude, which means the magnetic south pole receives more sunlit than the magnetic north Pole in average. The ratio in the southern

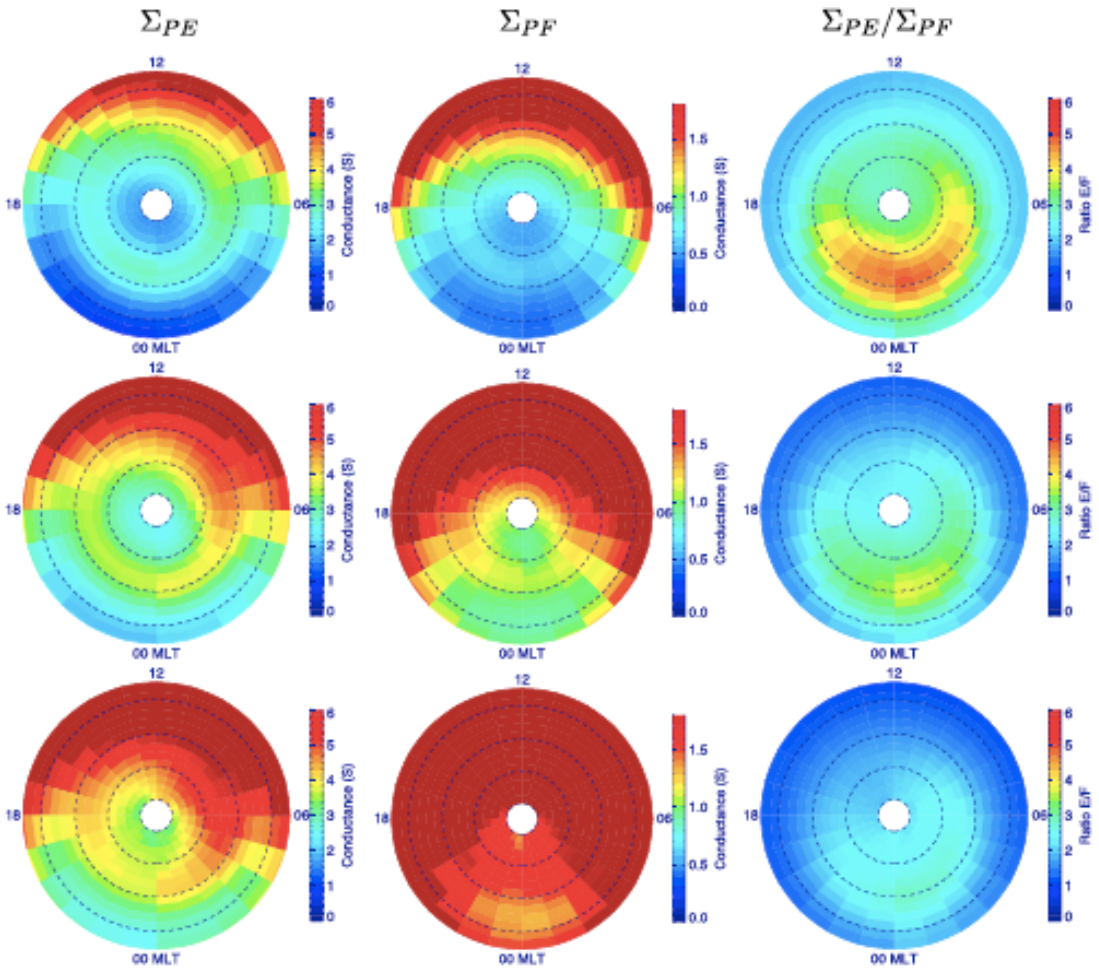

Figure 2.7 Similar to the figure 2.6, but for the southern hemisphere

hemisphere is smaller than in the norther hemisphere in all conditions. In Sheng et al. [2014], an inter-hemispheric asymmetry that the seasonal variation of the ratio between Σ_{PE} and Σ_{PF} is larger in the Southern Hemisphere than in the northern hemisphere has been recognized. In this part, we further examine the interhemispheric asymmetry and focus on the local time dependence. Similar to the procedure in section 2.3, the dependence of Σ_{PE}, Σ_{PF}, and

the ration on the F10.7 index at the center of the nighttime aurora zone has been compared between the two hemispheres at two different local times, 02–03 MLT and 21–22 MLT, as shown in Figure 2.8.

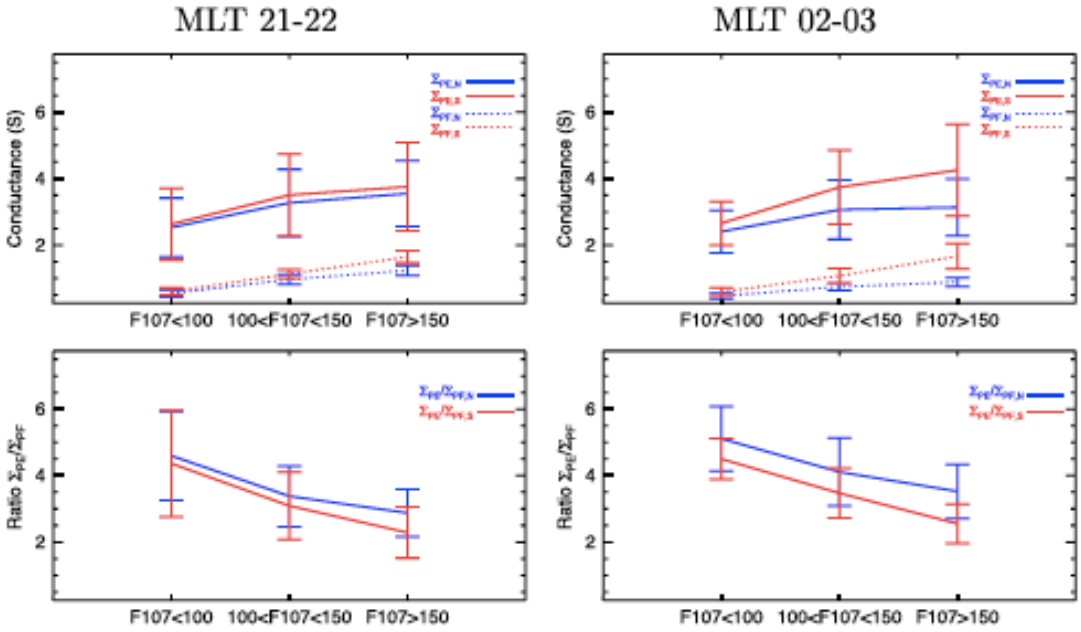

Figure 2.8. Similar to figure 2.5, comparisons of Σ_{PE}, Σ_{PF}, and their ratio (Σ_{PE}/Σ_{PF}) between the two hemispheres at (left column) MLT =21–22 and (right column) MLT = 02–03 under different solar activity conditions [Sheng et al., 2017].

Similar to figure 2.5, figure 2.8 shows Pedersen conductivity dependence of F10.7 index. The top row is the conductivity in the E region and F region. The bottom panel shows the ratio. The left part is the MLT 21-22 which is the pre-midnight sector and the right part is the MLT 02-23 which is the post-midnight sector. The blue line represents the northern hemisphere and red line represents the southern hemisphere. Again, the differences between two hemispheres in post-midnight sector (MLT 02-23) is larger than in the pre-midnight sector. And the Pedersen conductivity is larger in the southern

hemisphere than in the northern hemisphere while the ratio in the northern hemisphere is larger than in the southern hemisphere. It should be emphasized that the solar radiation is not equal between the aurora zones in the two hemispheres due to the tilt and shift of the geomagnetic poles. The aurora activity is not symmetric between the two hemispheres as well. Furthermore, even in the same hemisphere solar radiation and aurora activity are not evenly distributed between the pre-midnight and post-midnight sectors in the aurora zone. While the solar radiation is evenly distributed along geographical longitudes, the geomagnetic activity and aurora zone are oriented according to the geomagnetic coordinates, which were used to bin the data. All these factors may contribute to the local time dependence of the ratio and the interhemispheric asymmetry identified in this study.

2.5 Discussion and Summary

In this chapter, the COSMIC electron profile data from 2009-2014 are used to calculate the height integrated Pedersen conductivity in the E (100-150 km) region and the F (150-600 km) region. The Σ_{PE}, Σ_{PF}, and their ratio (Σ_{PE}/Σ_{PF}) in different Ap and F10.7 conditions have been analyzed. Altitudinal distributions of the Pedersen conductivity and energy deposition by Joule heating are crucial to accurate modeling of the neutral density response [e.g., Deng et al., 2013]. Both the solar activity and geomagnetic activity will control the Pedersen conductivity. The peak value in the aurora in both E region and F region increases whenever the Ap index increases or the F10.7 index increases. The ratio change shows a different trend for different conditions. When the

Ap index increases, the ratio will increase and ratio will decrease as the F10.7 index increases. This implies the geomagnetic activity main deposit the energy into the E region and solar activity influences the F region more. The change in the southern hemisphere tends to be larger than in the northern hemisphere since the southern magnetic pole will receive more sunlit. The interhemispheric asymmetry of Pedersen conductivity and ratio tend to have larger differences in the post-midnight sector than in the pre-midnight sector. The possible mechanisms for the interhemispheric asymmetry in ionospheric conductance and their ratio include unequal energy inputs between the two hemispheres and uneven solar radiation and aurora activity between the pre-midnight and post-midnight sectors in the aurora zone. The inter-hemispheric asymmetry and the local time dependences need further detailed studies of more data base.

```
```

CHAPTER 3

POYNTING FLUX IN THE DAYSIDE POLAR CAP BOUNDARY REGIONS

3.1 Introduction of polar cap boundary regions

In this chapter, the Poynting flux in the dayside polar cap boundary regions has been investigated, specifically in two regions, the cusp and the lower latitude boundary region (LLBL). In these regions, the energetic particles and electromagnetic energy from solar wind can gain direct entry to the magnetosphere and deposit into the upper atmosphere. The substantial amount of soft particle precipitation and Poynting flux energy are the most evident features of cusp and LLBL [*Heikkila et al.*, 1971; *Potemra et al*., 1977; *Deng et al*., 2015], which is the focus in this study. Moreover, the average energy and total energy flux of precipitating particles has commonly been utilized for the identification of the cusp and LLBL regions. Usually, if the average energy of ions is between 300 eV and 3 keV, the average energy of electrons is lower than 220 eV, and the total ion and electron energy fluxes are over 10^{10} eV/cm^2.s.sr and 6×10^{10} eV/cm^2.s.sr, the region is identified as cusp. If the average energy of ions is between 3 keV and 6 keV, the average energy of electrons is between 220 eV and 600 eV, and the total ion and electron energy fluxes are over 10^{10} eV/cm^2.s.sr and 6×10^{10} eV/cm^2.s.sr the region is identified as LLBL [*Newell and Meng et al*., 1988].

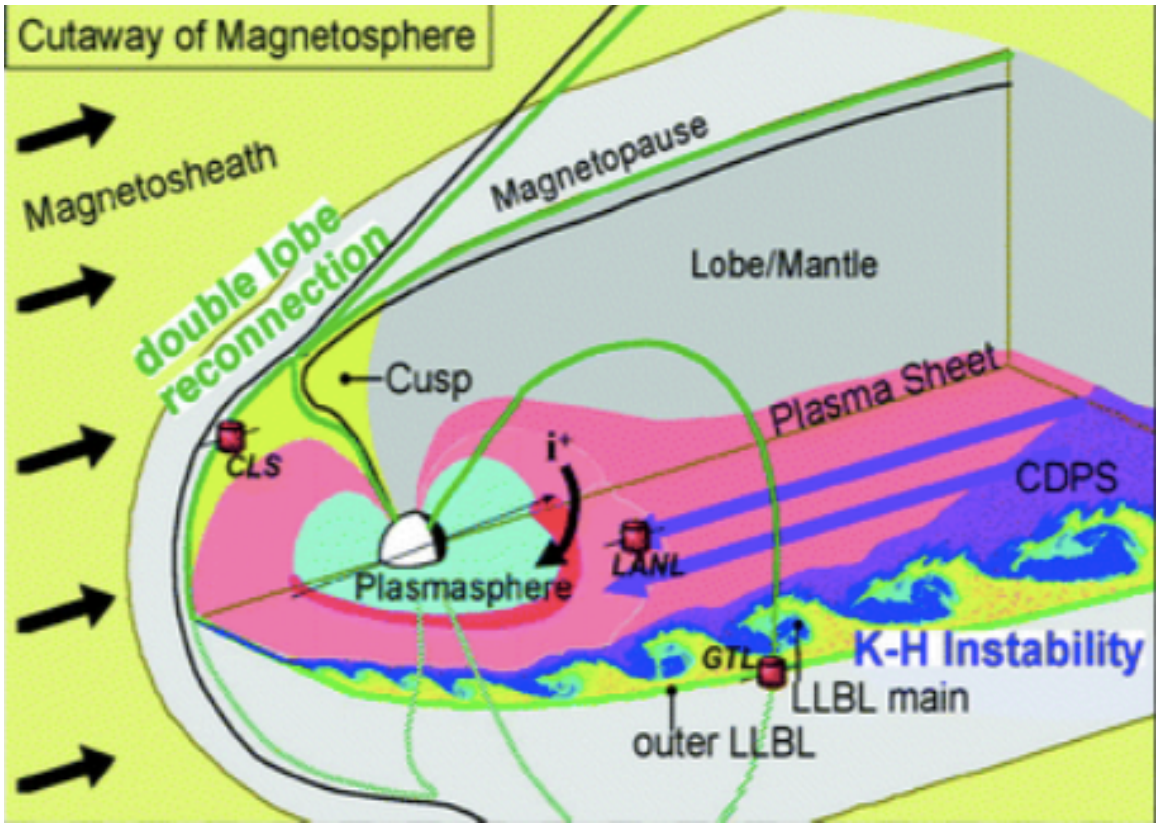

- Figure 3.1 The schematic view of the cusp and LLBL. (Courtesy of of Lavraud 2011)

Above figure 3.1 shows a schematic view of the location of the cusp and the LLBL in the magnetosphere. As it is mentioned above, the particle energy and Poynting flux energy could transfer to the ionosphere through the magnetic field line in these polar cap boundary regions. In this chapter, the Poyngtin flux and particle energy in these regions and their relationship have been calculated.

The soft particles precipitation and Poynting flux in the cusp and LLBL, which have important impact on the I-T system, are affected by solar wind conditions. For example, the intensity of soft particle precipitation has a strong dependence on the interplanetary

magnetic field (IMF) conditions [*Newell et al*., 2008]. The field line-integrated electromagnetic energy dissipated in the ionosphere is described by the Poynting flux flowing into the ionosphere through the ionospheric top boundary [*Kelly et al*, 2009; *Richmond et al.,* 2010]. Therefore, the DSMP satellites flying above 800 km altitude could provide important information of particle and electromagnetic energy inputs in the ionosphere especially in the cusp and LLBL regions. Previous observations from DMSP satellites showed a substantial amount of Poynting flux in the cusp and LLBL in the By dominant cases [*Knipp et al.,* 2011, *Deng et al*., 2015].

In this work a statistical study has been conducted using DMSP F15 satellite (800-850 km) observations. The DMSP data in the cusp and LLBL regions have been utilized to investigate the variation of Poynting flux energy in those polar cap boundary regions. The dependence of cusp Poynting flux on the IMF magnitude under different IMF orientations is discussed. The correlation between Poynting flux and the particle precipitation energy flux in both cusp and LLBL is examined as well. This work improves our understanding of the energy inputs in the dayside polar cap boundary regions and their correlation with geomagnetic conditions.

3.2 Data source and Methodology

In this chapter, the observations from DMSP F15 from year 2000-2004 have been used to calculate the Poynting flux. The Defense Meteorological Satellite Program (DMSP) is a Department of Defense(DoD) program run by the Air Force Space and Missile Systems

Center(SMC). The DMSP program designs, builds, launches, and maintains several near polar orbiting, Sun synchronous satellites monitoring the meteorological, oceanographic, and solar-terrestrial physics environments. The cross-track ion drift data are from Ion Drift Meter (IDM) of the Special Sensors-Ions, Electrons, and Scintillation (SSIES) monitor and the ram component ion drift data are measured by Retarding Potential Analyzer (RPA) The magnetic field is from Special Sensor Magnetometer (SSM) [*Kilcommons et al*., 2017; *Rich et al*., 1994]. Particle data from the Special Sensor for particles (SSJ-4) were obtained from Johns Hopkins University Applied Physics Laboratory (JHU/APL The Online Spectrogram Viewer developed by the JHU/APL has been used to identify the cusp and LLBL regions based on the DMSP particle data

It should be noticed that the SSJ 4 sensor on DMSP F15 has degraded low-energy ion detectors (30 eV – 1 keV), which may influence the identification of the cusp region. Since the low-energy detectors (<1 keV) on F15 are not trustworthy, only the cusp observations with the ion energy of the peak ion energy flux larger than or equal to 1.4 keV will be kept (1.4 keV is the mean energy in the 2nd band of the high-energy detector). Therefore, the average energy calculated by F15 is likely larger than 1 keV because the peak of particle energy spectrum is already in the band of the high-energy detector and the missing part of spectrum is only a low-energy tail. While the current F15 data do have some flaws, the results should still be meaninsgful if we discard all the cases in which the peak ion energy flux happens at the ion energy band < 1.4 keV in the cusp and LLBL. Meanwhile, our comparison with F16 data in 2004, which had a fully functioning SSJ5 instrument [*Redmon et al*., 2017], showed that with ~85% chance the ion average

energy in the cusp is >1 keV, which indicates that the ion particles above 1 keV contribute more than those below 1 keV in statistics.

Poynting flux is calculated from the formula of $\mathbf{S} = \mathbf{E} \times \delta\mathbf{B} / \mu_0$ [*Kelly et al*., 1991, *Knipp et al*., 2011; *Rastatter et al.,* 2016], where **E** is the electric field (cross and along-track components) and δ**B** is the magnetic field perturbation. The electric field is derived from ion drift velocity through the formula $\mathbf{E} = -\mathbf{v} \times \mathbf{B}$. The magnetic field perturbation is calculated by subtracting the background magnetic field from the observed magnetic field. At DMSP satellite altitudes, the IGRF model has been used to represent the background field. Therefore, the perturbation magnetic field δ**B,** is calculated by subtracting IGRF magnetic field from the observations ($\delta\mathbf{B} = \mathbf{B}_{measure}-\mathbf{B}_{IGRF}$) [*Huang and Burke et al*., 2004]. Here $\mathbf{B}_{IGRF}$ is the magnetic field vector produced by IGRF at satellite location and altitude, and $\mathbf{B}_{measure}$ is magnetic field measured by SSM. The subtraction is performed in the spacecraft coordinate frame, with the IGRF vector rotated into spacecraft frame from the geographic frame. More details could be found in *Kilcommons et al.,* [2017].

Quantifying the reliability of satellite observations, especially the Poynting flux, is challenging. The uncertainties in Poynting flux come from the uncertainties in the electric and magnetic fields. The uncertainty of electric field is related to the quality of both IDM and RPA data. The detailed information about the examination of the composition and convection pattern can be found in *Deng et al*., [2015]. The uncertainty of magnetic field can be introduced by the inaccuracy of spacecraft locations and artifact signals related to ring current, measurement artifacts and step-discontinuities in

the baseline. The ring current signal is the largest source of uncertainty and was removed using a polynomial fit technique. SSM data has been reprocessed to reduce those possible uncertainties [*Kilcommons et al.,* 2017]. Generally, the uncertainty in Poyngting flux is close to 25%-30% for high quality ion drift data observed in the cusp and LLBL [*Rastätter et al.,* 2016; *Kilcommons et al.,* 2017].

3.3 Results

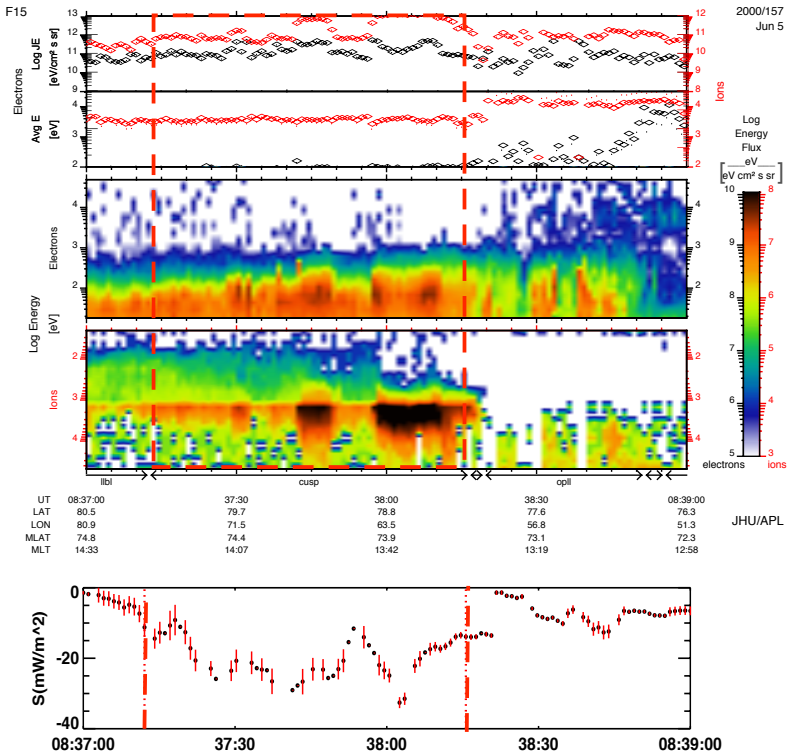

Figure 3.2: DMSP F15 observations on June 5th, 2000. The top panel shows ion energy flux observed by DMSP F15. The second panel shows average energy of ions. The third and fourth panel represent electron and ion spectrum respectively. The cusp region is bounded by the arrow and marked by the red box, which is between 80.5^0 and 78.8^0 latitudes with enhancement of ion and electron fluxes. The bottom panel shows the calculated Poynting flux during the same period and the cusp region is marked by the magenta dashed line. The negative value represents the downward (earthward) direction and noticeable downward Poynting flux, S, can be identified in the cusp region. The red bars are the error bars for Poynting flux [Lu *et al.*, 2018].

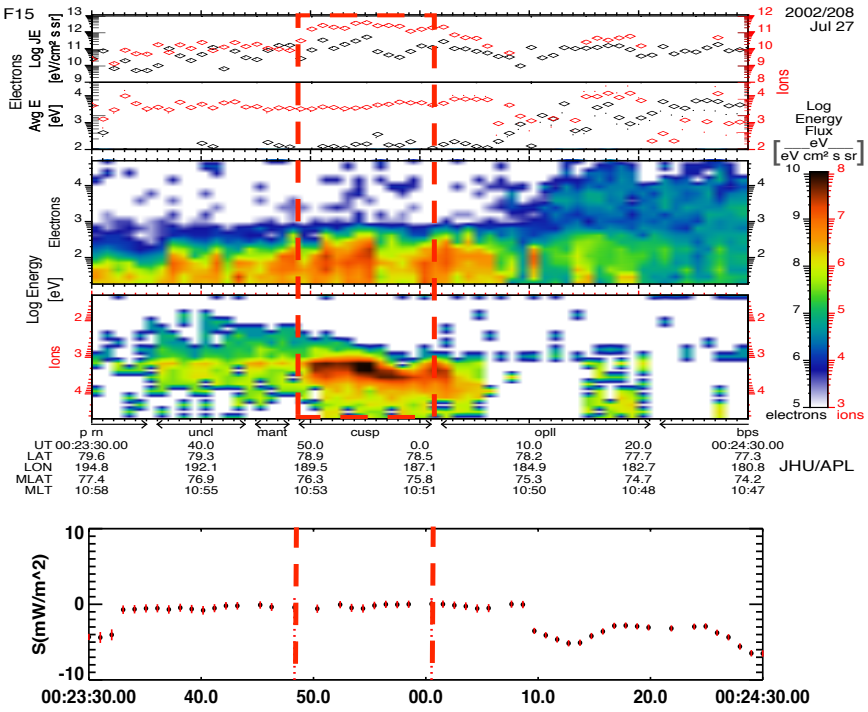

Figure 3.3: Same as Figure 1, excpet for DMSP F15 observations on 27 July, 2002. The Poynting flux in the cusp region was negligible. However, LLBL region showed noticeable downward Poynting flux, S [Lu *et al*., 2018].

Figure 3.2 shows a DMSP F15 cusp crossing on June 5, 2000. The red rectangle marks the period from 08:37:10 UT to 08:38:17 UT, when the satellite observed typical ion and soft electron enhancements in the cusp region. The bottom panel shows the Poynting flux calculated from F15 measurements with negative values representing downward Poynting flux. In the cusp region the maximum downward Poynting flux reached 35

mW/m^2. This case represents a situation that DMSP F15 observed strong Poynting flux in the cusp region. Figure 3.3 shows a DMSP F15 cusp crossing on July 27, 2002. The F15 satellite crossed the cusp region from 00:23:47 UT to 00:24:01 UT. In contrast, during this period the Poynting flux observed by F15 satellite was very small and no clear enhancement of Poynting flux can be identified in the cusp. This case represents a situation when DMSP F15 observed no clear Poynting flux in the cusp. In general, Figure 3.2 and 3.3 show that the DMSP F15 may or may not observe strong Poynting flux in the cusp, which represent two possible ways of Poynting flux variation in the cusp region. The IMF conditions have some differences for those two cases. For the first case By is dominant and Bz is negative (By = 5.54 nT, Bz = -3.56 nT), but for the second case By is negative and Bz is also negative (By = -0.74 nT, Bz = -1.86 nT) and much smaller than the first case. The statistical study of the IMF dependence is shown and discussed in the following paragraphs. It is also noticeable that the particle precipitation is different in those two cases. The correlation between Poynting flux and electron energy will be discussed in the following paragraphs as well.

The ionospheric and thermospheric perturbation can be quite different, depending on whether a substantial amount of Poynting flux in the cusp and LLBL exists or not. It is critical to determine the likelihood of having clear Poynting flux enhancements in the cusp and LLBL. In this statistical study, 660 cusp crossings and 11,461 LLBL crossings from DMSP F15 observations are processed.

Table 1

	cusp	llbl
S>10	350	4012
3<S<10	213	3913
1<S<3	48	2109
S<1	49	1427

Table 1 shows the number of cases observed by DMSP F15 in the cusp and LLBL regions for each category. The category is defined by the peak value of Poynting flux, S, in each crossing. For example, the category of S>10 means that that the peak value of Poynting flux in the region is more than 10 mW/m^2 [Lu *et al.*, 2018].

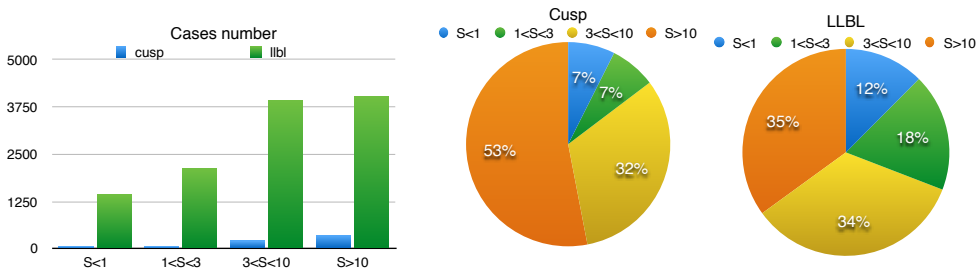

Figure 3.4: The histogram shows the number comparison between the cusp and LLBL in each category. The pie charts show the percentage of downward Poynting flux observations in each category. The left side is the cusp and the right side is the LLBL [Lu *et al.*, 2018].

Figure 3.4 shows a pie chart of the distribution of Poynting flux magnitudes observed in the cusp and LLBL regions. Table 1 shows the specific numbers in four different categories. Since *Gary et al*, [1995] reported average auroral zone Poynting flux value of ~10 mW/m2 for the DE-2 satellite observations, we define it as "strong Poynting flux" if the maximum Poynting flux observed in a cusp crossing is greater than 10 mW/m^2. As shown in Weimer [2005], Poynting flux in the dayside polar cap boundary regions is between 3 and 10 mW/m^2 climatologically. Therefore, we define it as "noticeable Poynting flux" if the maximum Poynting flux is greater than 3 mW/m^2 but smaller than 10 mW/m^2. If the energy input is lower than 1 mW/m^2, it typically becomes negligible and we define it as "no clear Poynting flux". If the Poynting flux is larger than 1 mW/m^2 but smaller than 3 mW/m^2 as happens <10% of the time in the cusp and < 20% in the LLBL, we call it "weak Poynting flux" and will not emphasize this category in this study in order to set a clear boundary between "noticeable Poynting flux" and "no clear Poynting flux" cases. As shown in Figure 3.4, for the 660 cusp crossings during 2000 to 2004, over half of cases (350) observed strong Poynting flux ($S > 10\ mW/m^2$), 32% cases observed noticeable Poynting flux ($3\ mW/m^2 < S < 10\ mW/m^2$), and only 7% cases observed no clear Poynting flux ($S < 1\ mW/m^2$). Meanwhile for LLBL region, 35% cases observed strong Poynting flux, 34% cases observed noticeable Poynting flux, and 12% cases observed no clear Poynting flux. The comparison between the cusp and LLBL regions reveals that there is a much higher chance to observe strong Poynting flux in the cusp region than in the LLBL. Clearly, the LLBL region has a higher chance to observe

"weak" and "no clear Poynting flux" than in the cusp region. The average Poynting flux in the cusp and LLBL are 12.7 and 7.8 mW/m^2, respectively. On average, Poynting flux in the cusp region is larger than that in the LLBL, which has been confirmed by the student t-test. It was shown with 90% certainty that the mean values of Poynting flux from DMSP F15 in the cusp were significantly larger than that from the same satellite in the LLBL.

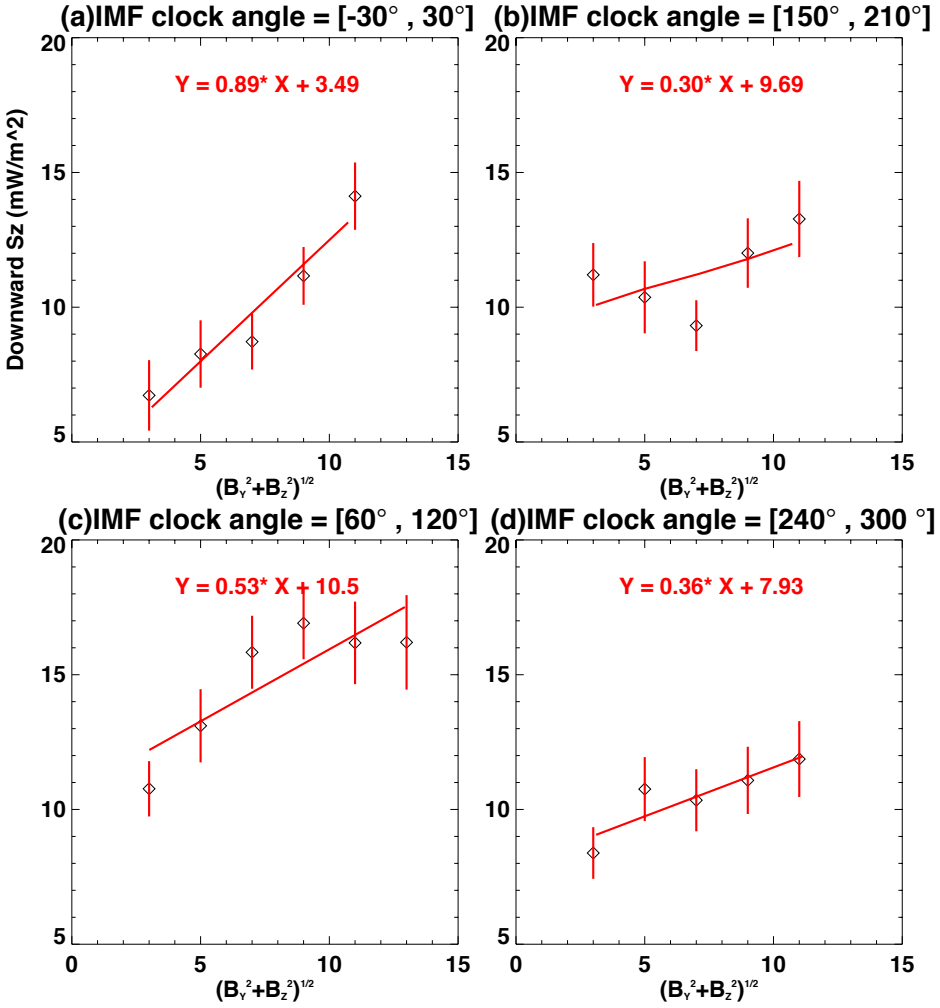

Figure 3.5: Correlation between IMF conditions and the maximum Poynting flux observed by DMSP F15 in the cusp region for different IMF clock angles, including (a) [-30º, 30º], (b) [150º, 210º], (c) [60º, 120º], and (d) [240º, 300º]. X axis is the magnitude of $\sqrt{\mathrm{By}^2 + \mathrm{Bz}^2}$ and Y axis is the Poynting flux. The Poynting flux data have been binned according to the magnitude of $\sqrt{\mathrm{By}^2 + \mathrm{Bz}^2}$. The diamond point represents the average and the vertical line shows the uncertainty of mean in each bin. The red line is the linear regression fitting to the average values. The correlations between X and Y are are (a) 0.95, (b) 0.59, (c) 0.83 and (d) 0.88, respectively. The number of observations in each part are (a) 66, (b) 174, (c) 135 and (d) 121, respectively [Lu *et al*., 2018].

The variation of Poynting flux with IMF conditions has been analyzed using the maximum value of Poyting flux in each cusp crossing and the corresponding IMF observations. The IMF data from OMNIweb (https://omniweb.gsfc.nasa.gov/ow_min.html) have been propagated to the bow shock nose (BSN) and a 5-minute delay has been included for the propagation from BSN to the upper atmosphere. Figure 3.5 shows that the correlation between the magnitude of IMF in the Y-Z plane ($\sqrt{\mathrm{By}^2 + \mathrm{Bz}^2}$) and the Poynting flux for four different IMF angles. The Poynting flux data have been binned according to the magnitude of $\sqrt{\mathrm{By}^2 + \mathrm{Bz}^2}$. and the width of each bin is 2 nT. In other words, the cases with IMF 2-4 nT are in one bin, as are the cases for IMF 4-6 nT, 6-8 nT, and so on. In Figure 3.5, the diamond points represent the average Poynting flux and the vertical lines show the uncertainty of the mean in each bin. The red lines are the linear regression fitting to the average values. Since it will not be statistically meaningful if the number of cases in a bin is too few, we only keep the bins with more than 10 cases. Therefore, the range of X-axis is ~ [2, 14] nT.

In Bz-dominant cases the correlation is stronger for northward Bz (Fig. 3.5a) than for southward Bz (Fig. 3.5b). In Bz northward cases, the slope of the fitting line is maximum (0.89) but the intercept is minimum (3.43), which indicates the Poynting flux in the cusp for northward Bz is small on average, even though it is very sensitive to the the change of IMF condition [*Cosgrove et al*., 2014]. When the IMF condition is By-dominant, the correlation calculated by a linear regression between Poynting flux and $\sqrt{\mathrm{By}^2 + \mathrm{Bz}^2}$ is 0.83 and 0.88 for By positive (Fig. 3.5c) and negative (Fig. 3.5d) conditions, respectively. For the By positive case, the intercept is maximum (10.9) and the slope is much larger than that in the By negative case (Figure 3.5d). The result of large Poynting flux in By-dominant cases is consistent with *Li et al*. [2011], who showed a substantial amount of Poynting flux in the dayside thermosphere under IMF By dominant condition.

The DMSP F15 spacecraft orbit is mainly in the 09-21 local time sector and therefore only a limited local time range is covered, nonetheless we have reason to believe that the large IMF By related differences in Poynting flux are real, with more downward cusp Poynting flux present during IMF By positive situations. Sandholt et al. [1992] noted that dayside auroral transients were favored under By positive conditions. Provan et al. [1999] reported that pulsed ionospheric flows observed by Finland's CUTLASS radar occurred more often when By was positive. The dayside Joule heating estimates shown in McHarg et al (2005) are higher for positive By. Xing et al. (2012) showed a tendency for higher occurrence of poleward moving auroral forms for By positive. All of these reports align with the idea put forth by Saunders [1989] that upward field aligned currents (FACS) dominate in the northern hemisphere cusp during positive By

conditions. The precipitating electrons required to support these FACs create dayside discrete auroral forms that move in enhanced flow channels. Sandholt and Farrugia [2007] showed the FACS, localized convection asymmetries and flow channels that are likely associated with the preferential enhancements of northern hemisphere Poynting flux during IMF By positive conditions reported here. Development of such a channel is illustrated for a sudden By negative to By positive rotation in Eriksson et al. (2017).

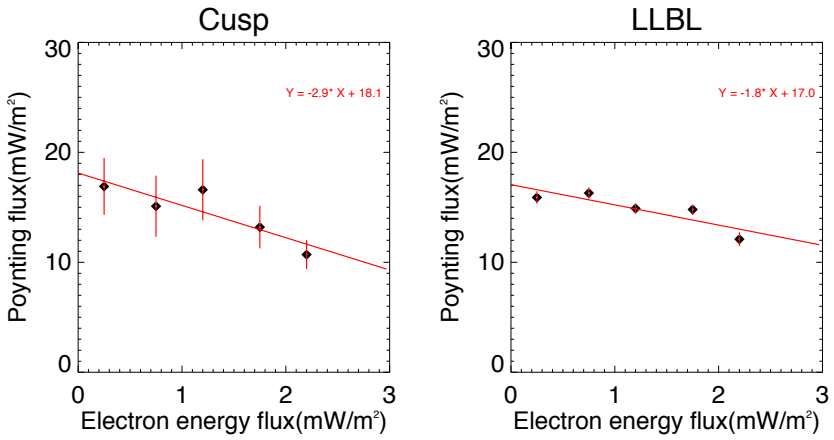

Figure 3.6: The correlation between Poynting flux and electron precipitation energy flux. The x-axis is the electron precipitation energy flux and the y-axis is the Poynting flux from DMSP F15. The Poynting flux data have been first binned according to the electron energy flux. The diamond represents the average of Poynting flux and the black line for each point is the uncertainty of mean in each bin. The red line is the linear regression fitting to the average [Lu *et al.*, 2018].

Figure 3.6 shows the correlation between Poynting flux and electron particle precipitation energy flux in the cusp and LLBL regions. The left side is for the cusp and

the right side is for the LLBL. The x-axis is the electron precipitation energy flux and the y-axis is the Poynting flux from DMSP F15. Similar to Figure 3.5, the Poynting flux data have been first binned according to the electron precipitation energy flux. The width of each bin is 0.5 mW/m^2 of electron energy flux. The diamond represents the average Poynting flux and the vertical line shows the uncertainty of mean in each bin. The red lines are the linear regression fitting to the average. The figure shows that for both cusp and LLBL regions, the Poynting flux decreases as the electron precipitation energy flux increases. The slope of red lines are -2.9 for the cusp region and -1.8 for the LLBL region, which indicates that the correlation between Poynting flux and electron precipitation energy flux is more sensitive in the cusp region than in the LLBL region. The negative correlation may be explained as the conservation of energy. It has been shown that dayside cusp aurora is caused by the particles from magnetosheath, which are accelerated by the waves along the field line due to the wave-particle interaction [Mende, et al., 2016]. When the acceleration is enhanced, more energy is carried by the particle precipitation and the Poynting flux can be reduced.

3.4 Summary and Discussion

In this study the Poynting flux in the cusp and LLBL regions is investigated through analyzing data from DMSP F15 satellite at ~850 km. The statistical results show that 53% of 660 DMSP cusp crossings observed strong downward Poynting flux ($S > 10mW/m^2$) in the cusp, 32% of the crossings had noticeable downward Poynting flux ($3mW/m^2 < S < 10mW/m^2$), and only 7% of the crossings did not show clear Poynting

flux ($S < 1mW/m^2$). A similar analysis has been conducted for the DMSP observations in the LLBL region. Thirty five % of 11461 LLBL crossings showed strong downward Poynting flux ($S > 10mW/m^2$), 34% of the crossings had noticeable downward Poynting flux ($3mW/m^2 < S < 10mW/m^2$), and 13% of the crossings did not show clear Poynting flux ($S < 1mW/m^2$). The statistical results indicate that the average electromagnetic energy input into the LLBL region is less than that in the cusp region. Since IMF conditions play a very important role in controlling the energy input into the geospace environment, the correlation between the Poynting flux in the cusp and the IMF conditions has also been analyzed. While the sensitivity of Poynting flux to the magnitude of IMF in the Y-Z plane is maximum during northward IMF conditions, the average Poynting flux is largest when By is dominant and positive, consistent with cusp upward FACs and enhanced pre-noon flow channels during such conditions. The Poynting flux and electron precipitation energy flux have a negative correlation in both cusp and LLBL region, which is more sensitive in the cusp region than in the LLBL region.

CHAPTER 4

GITM SIMULATION OF SAPS EVENT IN A GEOMAGNETIC STORM

4.1 Methodology: GITM model

In this chapter, we have utilized the Global Ionosphere Thermosphere Model (GITM) [Ridley *et al*., 2006] to study a geomagnetic storm event in the March 17th 2013. GITM is a 3-dimensional spherical code that models the Earth's thermosphere and ionosphere system using a stretched grid in latitude and altitude. The number of grid points in each direction can be specified, so the resolution is extremely flexible. GITM explicitly solves for the neutral densities of O, O2, N(2D), N(2P), N(4S), N2, and NO; and ion species O+(4S), O+(2D), O+(2P), O2+, N+, N2+, and NO+. One major difference between GITM and other thermosphere codes is the use of an altitude grid instead of a pressure grid. The vertical grid spacing is less than 3 km in the lower thermosphere, and over 10 km in the upper thermosphere. GITM allows for non-hydrostatic solutions to develop (i.e., the full vertical momentum equation is solved) [Deng *et al.*, 2008], so more realistic dynamics in the auroral zone can be simulated. GITM includes a modern advection solver and realistic source terms for the continuity, momentum, and energy equations. Each neutral species has a separate vertical velocity, with coupling of the velocities through a frictional term. The ion momentum equation is solved for assuming steady state, taking into account the pressure, gravity, neutral winds, and external electric fields. GITM is coupled to a large number of models of the high-latitude ionospheric electrodynamics, for example, the assimilative mapping of ionospheric electrodynamics (AMIE) technique, Weimer, Foster, Heppner and Maynard or Ridley et al.

electrodynamic potential patterns. In the default GITM runs, Weimer05 is used to specify high latitude electric potential, Fuller-Rowell and Evans [1987] is used to specify the aurora, and MSIS and IRI are used to set the initial state. GITM currently covers all latitudes and a vertical range from about 110 km to 600 km.

As mentioned above, we need some forcing such as convection pattern and particle precipitation to drive the GITM model. In general, the forcing is specified using empirical models. The empirical model can represent climatologically average situation very well, however, it could not capture the localized small structures . To study the geomagnetic storm at March 17th 2013 which is also called as St.Patrick storm, we need more specific forcing to simulate the real event. In the following paragraphs, we will use the observations from DMSP F18 and output of Rice Convection Model (RCM) to drive the GITM.

4.2 Introduction of the SAPS event

Sub-aurora polarization stream (SAPS) is a term introduced by Foster and Burke [2002] to describe strong westward plasma flows in the mid-latitude ionosphere equatorward of the aurora convection zone. SAPS flows tend to be latitudinally narrow and are predominantly observed in the dusk-midnight sector, either just equatorward or at the edge of the auroral oval [Anderson et al., 1993, 2001; Parkinson et al., 2005; Koustov et al., 2006; Oksaviket al., 2006; Makarevich and Dyson, 2008; Grocott et al., 2011; Kunduri et al., 2012]. SAPS is an important feature of magnetosphere-ionosphere-thermosphere coupling that strongly influences the evolution of large-scale features in the mid-latitude

ionosphere such as the formation of density troughs [Spiro et al., 1978] and storm enhanced density/plasmaspheric plumes [Foster et al., 2002; Goldstein et al., 2004; Thomas et al., 2013]. Some of the earliest observations of strong westward flows in the sub-auroral ionosphere were reported by Galperin et al. [1974], and these flows were typically associated with substorm activity [Southwood and Wolf , 1978; Spiro et al., 1979]. More recent studies on SAPS [Anderson et al., 1993, 2001; Huang and Foster , 2007; Erickson et al., 2011] indicate that they are predominantly associated with disturbed geomagnetic conditions during which the equatorward edge of the ion precipitation boundary moves equatorward of the electron precipitation boundary [Gussenhoven et al., 1987; Heinemann et al., 1989]. This misalignment in the boundaries is thought to produce a polarization electric field. Another consideration is that, Region-2 field aligned currents (FACs) flow into the region collocated with the ion precipitation boundary in the pre-midnight sector of the ionosphere [Klumpar , 1979; Anderson et al., 1993] and close with Region-1 FACs via the poleward-directed Pedersen currents. However, this current closure is hindered by the low conductivity of the sub-auroral ionosphere, resulting in large poleward-directed electric fields leading to the westward-directed EXB drifts observed in SAPS [Anderson et al., 1993]. The Region-2 FACs are driven by pressure gradients inside the ring current [Toffoletto et al., 2003] and these variations can have an influence on the electric fields in the SAPS channel [Clausen et al., 2012a]. Additionally, Anderson et al. [1993, 2001] suggested that the strong electric fields result in a decrease in the conductivity of the region [Schunk et al., 1976; Banks and Yasuhara, 1978] producing a positive feedback effect

that allows the electric fields to grow even more. Zheng et al. [2008] used models of the mid-latitude trough and ring current to demonstrate that the low conductance in the sub-auroral region is critical to the large amplitudes observed in SAPS. Statistical characterization of SAPS in the literature has primarily been based on measurements from either the ion drift meter (IDM) instrument onboard Defense Meteorological Satellite Program (DMSP) satellites [Wang et al., 2008] or the Millstone Hill incoherent scatter radar [Foster and Vo, 2002; Erickson et al., 2011]. Wang et al. [2008] investigated the effects of cross polar cap potential, conductivity integrated over sub-auroral flux tubes, and Dst on SAPS and found an exponential relationship between SAPS latitude and Dst. Foster and Vo [2002] analyzed two decades of Millstone Hill incoherent scatter radar (ISR) data and characterized the average magnetic latitude (MLAT)-magnetic local time (MLT) location of SAPS for different Kp index levels. A subsequent study by Erickson et al. [2011] found that the latitude of SAPS peak velocity decreases as a function of Dst and MLT.

4.3 DMSP observations

The Defense Meteorological Satellite Program (DMSP) is a Department of Defense(DoD) program run by the Air Force Space and Missle Systems Center(SMC). The DMSP program designs, builds, launches, and maintains several near polar orbiting, Sun synchronous satellites monitoring the meteorological, oceanographic, and solar-terrestrial physics environments. DMSP satellites are in a near polar orbiting, Sun

synchronous orbit at an altitude of approximately 830 Km above the Earth. Each satellite has an orbital period of about 101 minutes. Each DMSP satellite monitors the atmospheric, oceanographic and solar-geophysical environment of the Earth. The space environmental sensors record along track plasma densities, velocities, composition and drifts. In this study, we use the data from DMSP F18 SSJ4 and SSIES. The DMSP SSJ/4 instruments monitor the energy flux of electrons and ions that precipitate from the Earth's magnetosphere. The DMSP SSIES instruments measure the ion drift. In this study, we will use the data of particle precipitation and ion drift from DMSP F18 instead of empirical model to drive the GITM. The advantage is that in the localized region, especially along the satellite track, the forcing is much close to the reality. The disadvantage is that in our simulation, we should assume that the forcing is constant (no time variation) during one track.

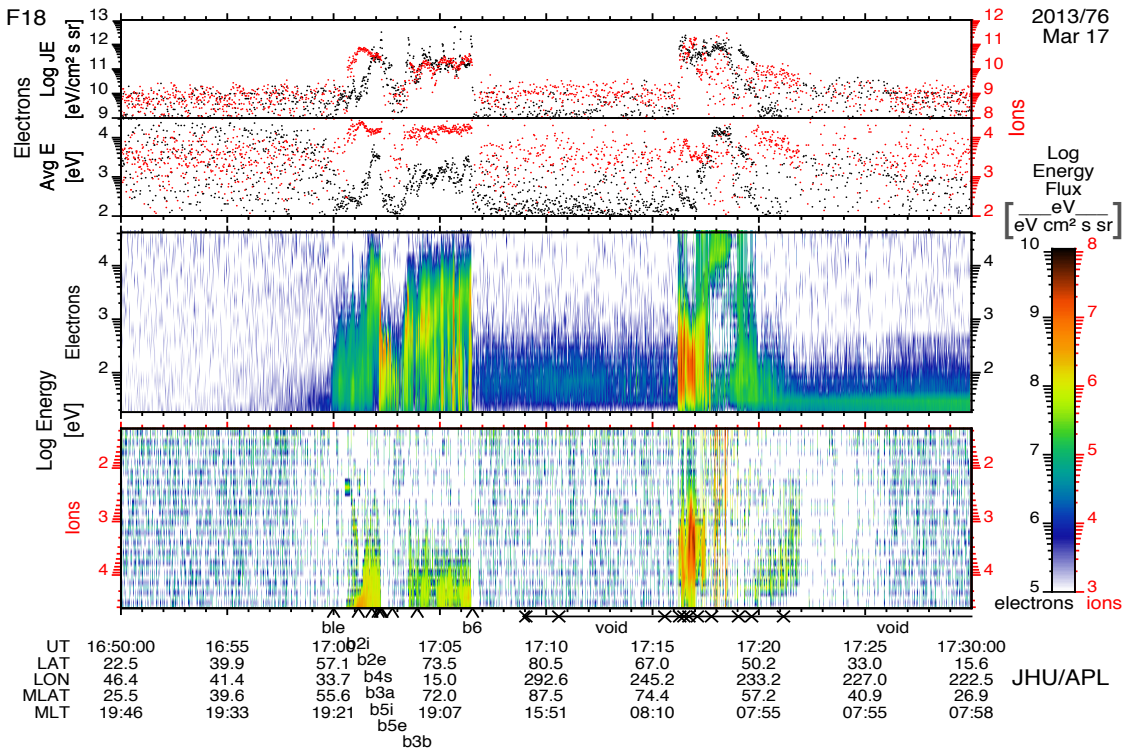

Figure 4.1: The DMSP F18 SSJ4/5 observation from 1650UT to 1730UT March 17th 2013 (Courtesy of JHU/APL).

Figure 4.1 shows the observations from DMSP F18 in our simulation time from 1650UT to 1730 UT March 17th 2013. The top two panels show the electron and ion energy flux and average energy. The black dots are electrons and red dots are ions. The bottom two panels show the electron and ion spectrum. In the aurora zone, the particle precipitation is enhanced. We could notice the satellite first cross the aurora near 1700 UT. We have used the data of electron energy and electron average energy along the satellite track to specify the particle precipitation in the GITM simulation.

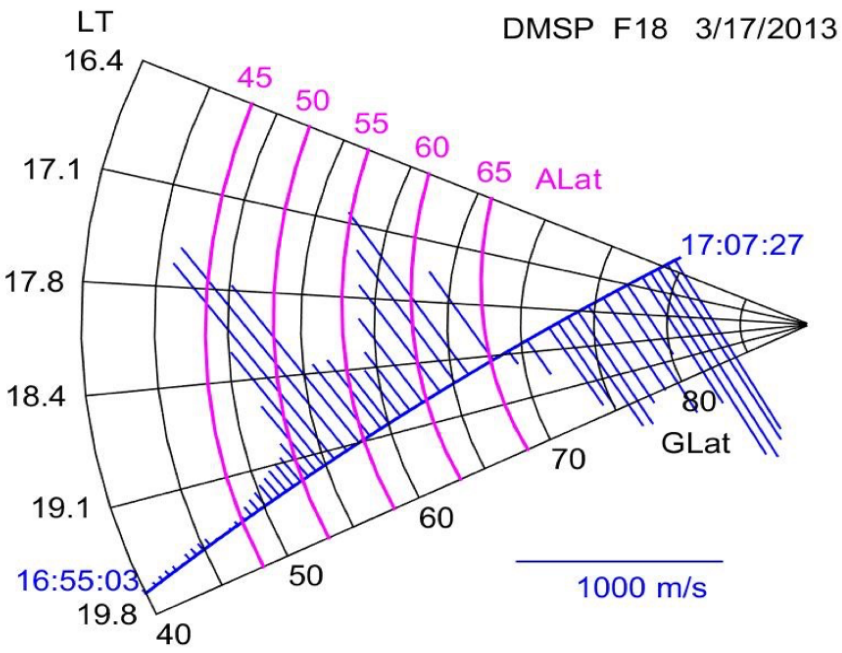

Figure 4.2 The ion drift observation from DMSP F18 March 17th 2013.

Another forcing is the convection, which has been specified by the data from SSIES. Above figure 4.2 shows the ion drift observed by DMSP F18 during our simulation time. The blue line represents the ion drift velocity from the observations. It is typical to have a strong sunward flow in the aurora region and an anti-sunward flow in the polar region due to the large-scale two-cell ion convection pattern. We should also notice that in the sub-aurora region at 55^0 and equatorward (several degrees south to the aurora equator boundary), there also exists a strong westward flow on the dusk side. This phenomenon is distinguished to the two-cell convection and is called as the SAPS. In our simulation, we have also used the convection pattern from DMSP F18 observations to replace the empirical model. One important part we need emphasize is that we only replace the

forcing from the background empirical models with DMSP data along the satellite track and leave the other places the same as the background from the empirical models. Therefore, the global forcing pattern may have some discontinuity at the boundary of satellite pattern and background pattern.

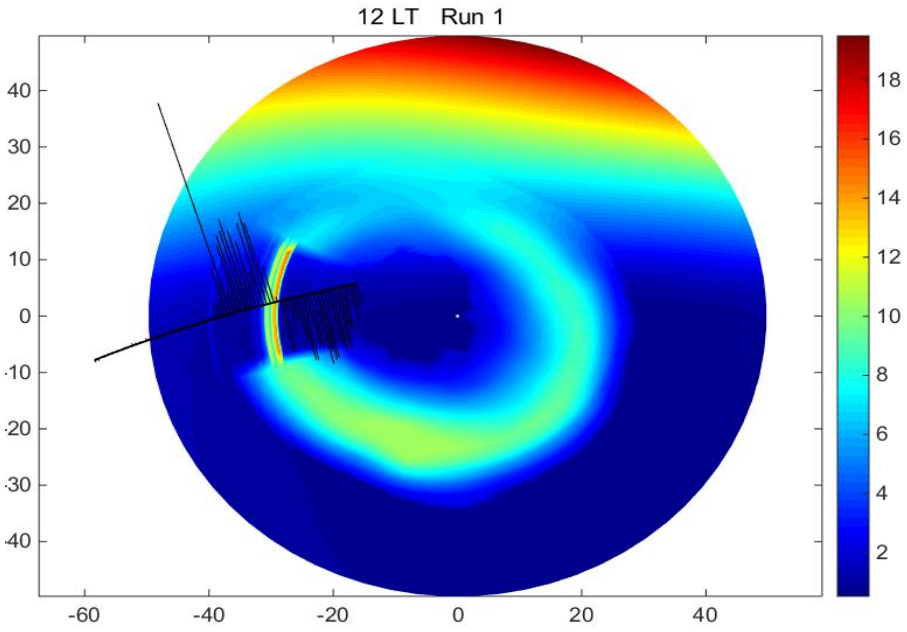

Figure 4.3 The forcing pattern specified in GITM for the March 17th 2013 SAPS simulations.

Above figure 4.3 shows the global forcing specified in GITM for the March 17th 2013 SAPS simulations. The background color represents the electron precipitation and the black line represents the ion drift. We can identify the smooth aurora from the empirical model and sharp intense aurora along the satellite track.

4.4 Eelctrodynamic forcing from RCM

As we mentioned before, empirical models could not capture the localized future especially during the geomagnetic storm time. One method is to use the DMSP observations to replace the forcing from the empirical models along the satellite trajectory. As previous paragraphs discussed, the replacement also brings some discontinuities and the forcing does not have the temporal variation during one period of the satellite fly. Therefore, it limits our simulation capability. In this chapter, we will introduce another forcing which comes from the outputs of Rice Convection model (RCM) [citation **].

The RCM is a bounce averaged-drift kinetic model related to the ring current and inner plasma sheet and their coupling to the ionosphere. It assumes an isotropic distribution function for all magnetospheric particles and calculates the temporal and spatial variation of the phase space density in the inner-plasma-sheet and ring current. The model considers particle drift in an inputted, time varying magnetic field, and a self-consistent potential electric field that is computed taking into account current closure in the ionosphere. It solves the transport equation, current conservation equation and potential equation. Auroral enhancements due to energetic particle precipitation are evaluated from the computed magnetospheric distribution function assuming loss rates that are a fraction of the strong pitch-angle scattering limit rate, and conductance values are estimated using the expressions of Robinson et al. (1987). Thus, it provides us the capability to use the particle precipitation and potential pattern to drive GITM. We also need to specify the inputs for RCM as well. In this study, we use the observations from Geotail satellite during the storm time to specify the initial particles at the RCM

boundary which is located at the magnetotail. Since the RCM is a physics-based model, we could get the outputs at every time step. Compared to DMSP forcing, the RCM forcing have a more continuous global pattern and temporal variation, although at the localized region especially along the satellite trajectory the RCM outputs is not as accurate as the observations.

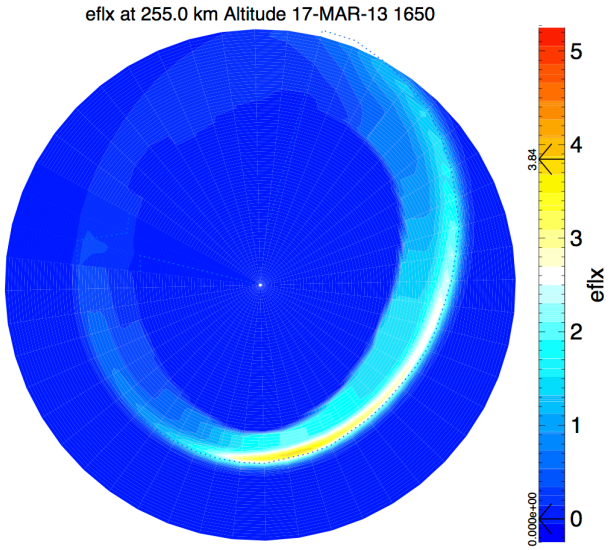

Figure 4.4 The electron energy flux from RCM output at 1650UT on March 17th 2013.

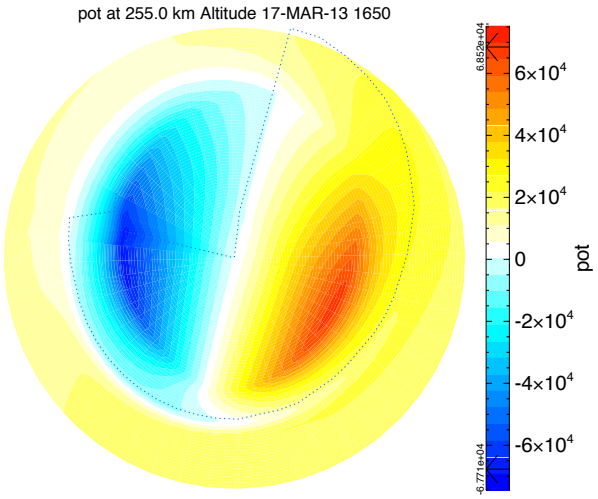

Figure 4.5 The potential pattern from RCM output at 1650UT on March 17th 2013.

The figure 4.4 and figure 4.5 show the potential pattern and electron precipitation from RCM simulation at 1650 UT on March 17th 2013. It is noticeable that the aurora zone from RCM output is narrower than the empirical model. The forcing from RCM simulation outputs, including both particle precipitation and potential pattern have been also used to driven the GITM model and the forcing patterns have been updated every 10 minutes.

4.5 GITM simulation results

As we discussed above, two different ways to drive GITM high-latitude electrodynamics have been used. The first method is to use the data from DMSP F18 observations. In this method, we have simulated the St.Patrick 2013 storm from 1650UT to 1730 UT. Figure 4.6 below shows the Dst index during the storm time. The Dst index represents the

average disturbance of magnetic field at the Earth surface near the equator. Therefore, the lager absolute value of Dst, the stronger the geomagnetic storm.

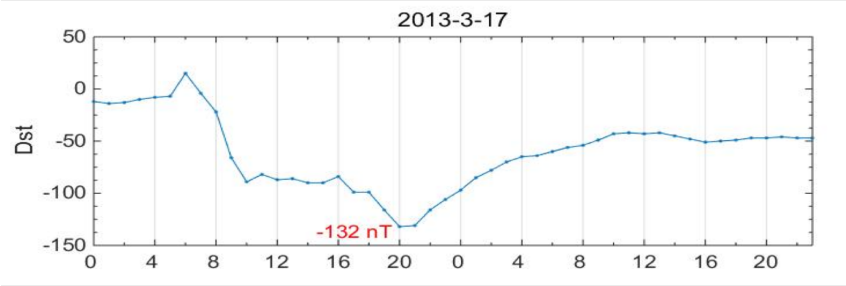

Figure 4.6 Dst index during March 17-18, 2013 storm.

From above figure 4.6, during the 05-06 UT on March 17th 2013, the Dst index increased. This time is defined as the initial phase of the geomagnetic storm. After that, from 06 UT to 20 UT, the Dst index decreased to -132 nT. This period is defined as the main phase. After the main phase, the Dst index increased again until the next day, and that period is called the recovery phase. We could notice during March 18th 2013, the Dst index was still negative. Actually, the recovery phase can usually last several days sometimes even up to 7 days. In this study, the simulation time from 1650 UT to 1730 UT on March 17th 2013 is during the main phase.

The figure 4.7 below shows the variation of neutral wind and ion drift along the DMSP trajectory. The bottom panel shows the ion drift which is the forcing specified by the

DMSP observations and the top panel shows the neutral wind from the GITM simulations. Using DMSP data, we run GITM for two different cases. One is the run with SAPS and the other one is without SAPS. The difference between these 2 runs is only the forcing located in the SAPS region. From the DMSP F18 SSJ observations showed previously, we could identify the aurora equatorward boundary. Based on the observations, at the southward of the aurora equatorward boundary is the sub-aurora region. The run with SAPS we use the DMSP data along the whole trajectory during the simulation time. And the run without SAPS we use the DMSP data along the track except at the sub-aurora region, where a simple linear interpolation has been used to remove the SAPS artificially. Therefore, the difference between those two cases shows the influence of SAPS to the thermosphere at the sub-aurora region.

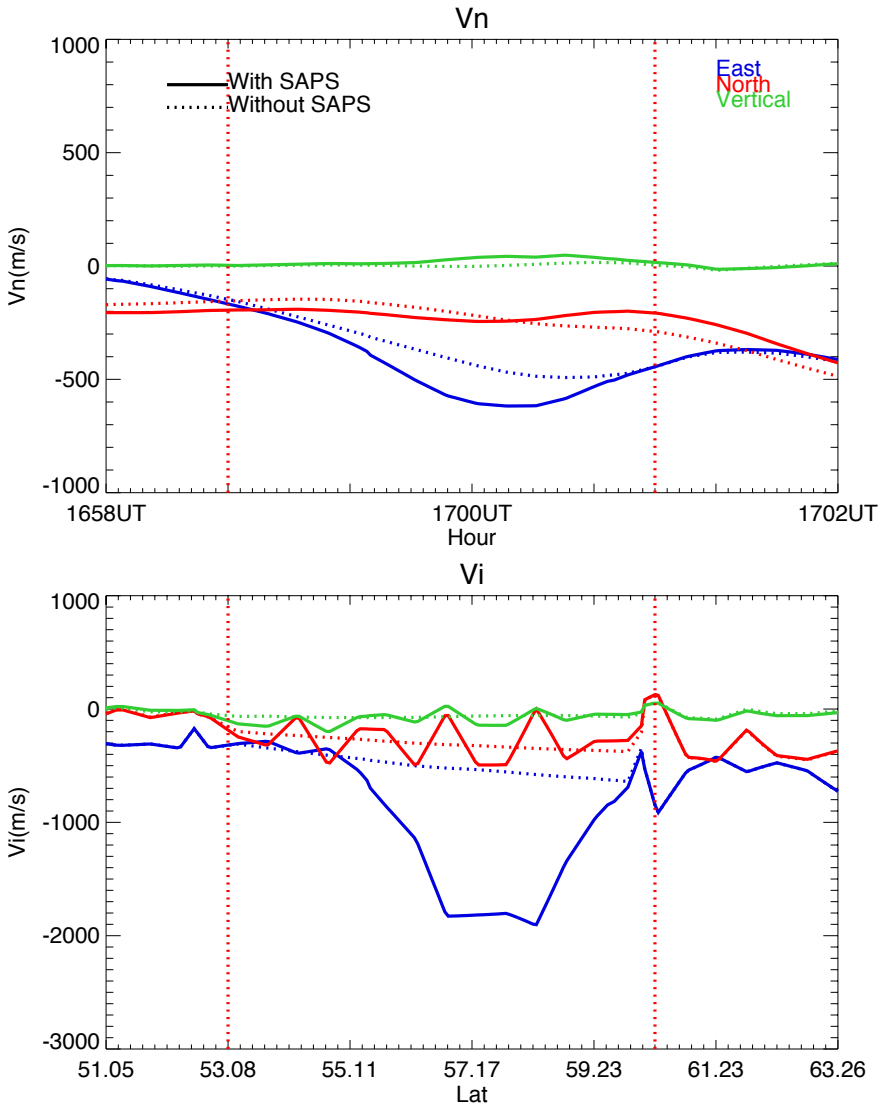

Figure 4.7 The GITM simulations of neutral wind and the ion drift from DMSP drive on March 17th 2013. The solid line is the run with SAPS while the dash line is the run without SAPS. The blue lines, red lines and green lines represent the eastward, northward, vertical direction respectively. The bottom panel is the ion drift which is the forcing.

Not surprisingly, the differences between the run with SAPS and without SAPS is the westward ion drift, since SAPS is westward on the duskside. The top panel, is the neutral wind along the DMSP trajectory from GITM simulation. It is obvious that the westward neutral wind with SAPS increased by ~100-150 m/s. Meanwhile, the neutral wind in the meridional direction also changed. The change due the influence of SAPS tends to have a strong latitude dependence. At the equatorward of sub-aurora, the neutral wind difference is southward and at the polarward os sub-aurora, the neutral wind difference is northward. The magnitude of neutral wind difference in the north-south direction is around 50 m/s and smaller than that in the east-west direction.

From the Newton 2nd law, we know that the neutral wind change is due to the momentum equation. The forces exerted on the neutral wind have many aspects including the pressure gradient force, Coriolis force, ion drag force and viscosity force. Since the GITM solves the momentum equation, it provides us the capability to study those force terms in detail.

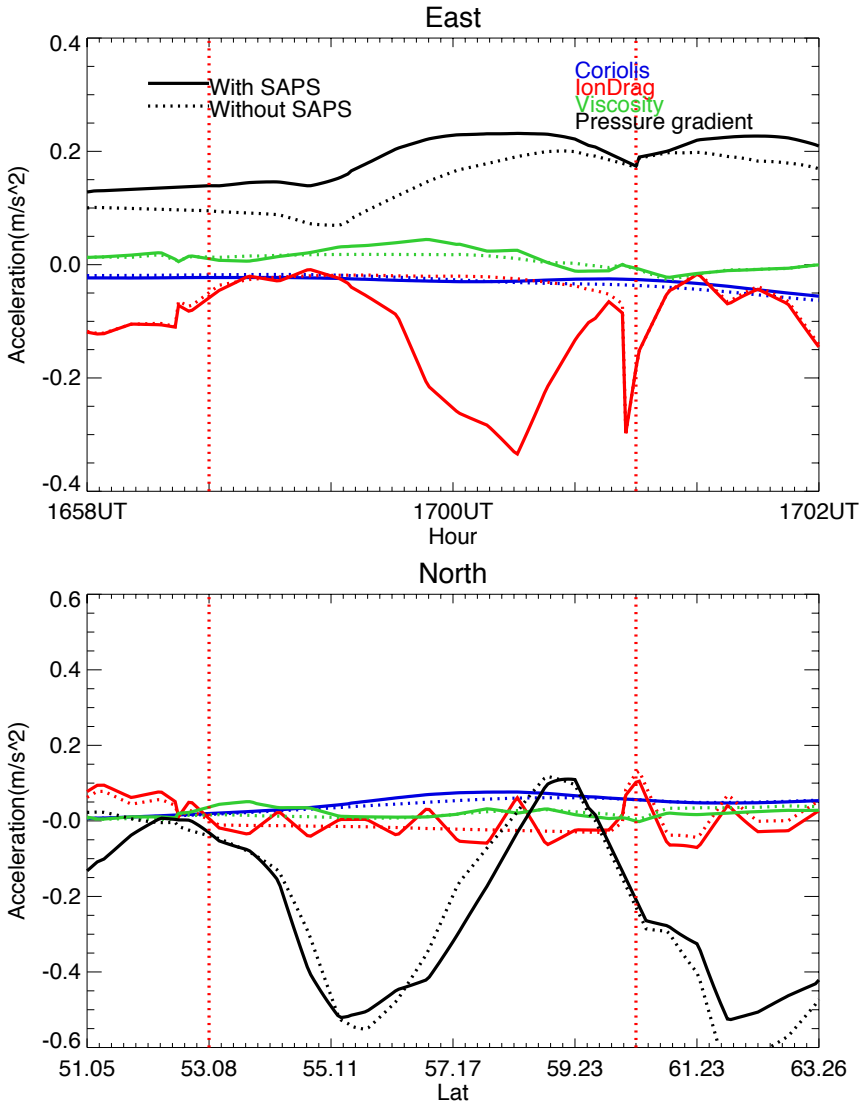

Figure 4.8 Force terms in the GITM simulations along the DMSP trajectory on March 17th 2013.

Above the figure 4.8 shows the different force terms along the satellite trajectory. Similar to the figure 4.7, the solid lines represents the case with SAPS and the dash lines represents the case without SAPS. We analyzed the four important forces and how they change along the satellite track. The top panel shows the force terms in the east-west

direction and the bottom panel shows the force terms in the north-south direction. The blue line, red line, green line and black line represents the Coriolis force, ion drag force, viscosity force and pressure gradient force, respectively. At the east-west direction, the pressure gradient force and the ion drag force are dominant. The SAPS increased the westward ion drag force significantly, because the high speed westward ion drift makes the differences of ion and neutral velocities much larger. Meanwhile, the SAPS increased the eastward pressure gradient force. The pressure gradient force is comparable to the ion drag force. The viscosity force changed to eastward as well. The Coriolis force is relatively small in the east-west direction. It is not a surprise, because the east-west Coriolis force is proportional to the northward flow, and the speed of origin northward flow is small. In the north-south direction, the pressure gradient force is dominant. The change of pressure gradient force due to SAPS effects is not as large as that in the east-west direction and tends to have a latitude dependence as well. The change of Coriolis force is in northward direction. Although the westward flow is strongly enhanced, the Coriolis force is still much smaller than the pressure gradient force.

In the following paragraph, we will discuss the GITM simulation results from the second specification, driven by RCM. If we use the forcing from DMSP data, the simulation results will only be trustable along the DMSP trajectory. But from the RCM forcing, we could have a global picture. In the RCM-driven run, our simulation time is from 00 UT to 24 UT on March 17th 2013. We update the forcing from RCM outputs every 10 minutes. Therefore, we could examine the formation and evolution of SAPS. Below the figure 4.9

and figure 4.10 show the GITM simulations driven by RCM. The arrows show the ion drift and neutral wind for figure 4.9 and figure 4.10, repsectively. The color background is the electron precipitation which helps to identify the aurora zone and aurora boundary.

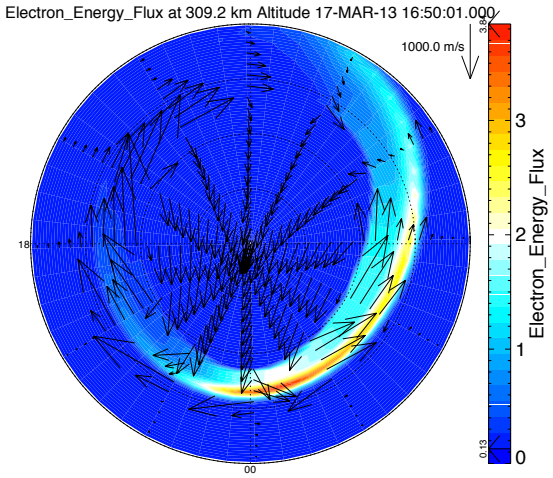

Figure 4.9 Ion drift from RCM to drive GITM at 1650UT on March 17th 2013.

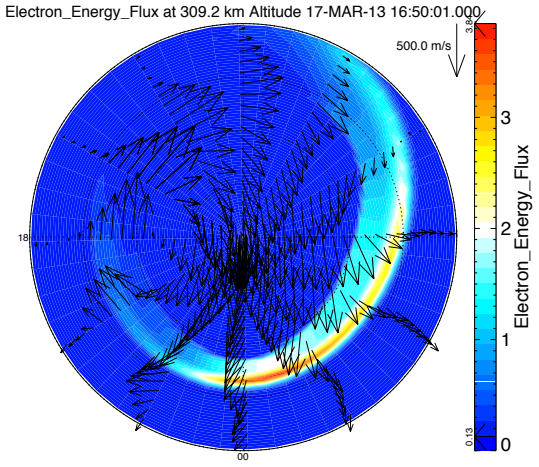

Figure 4.10 The GITM simulation results of neutral wind driven by RCM at 1650UT on March 17th 2013.

The GITM simulation results showed above is at 1650 UT. It is close to the start time of simulation in our first approach using DMSP observations. It is noticeable that there exist a strong west-ward ion drift on the dusk side near the sur-aurora region in addition to the large scale two cell convection. Usually, the SAPS event tends to appear on the dusk side more often than other locations; therefore we extract the parameters from GITM simulations at a fixed local time and examine the evolution of the SAPS with time.

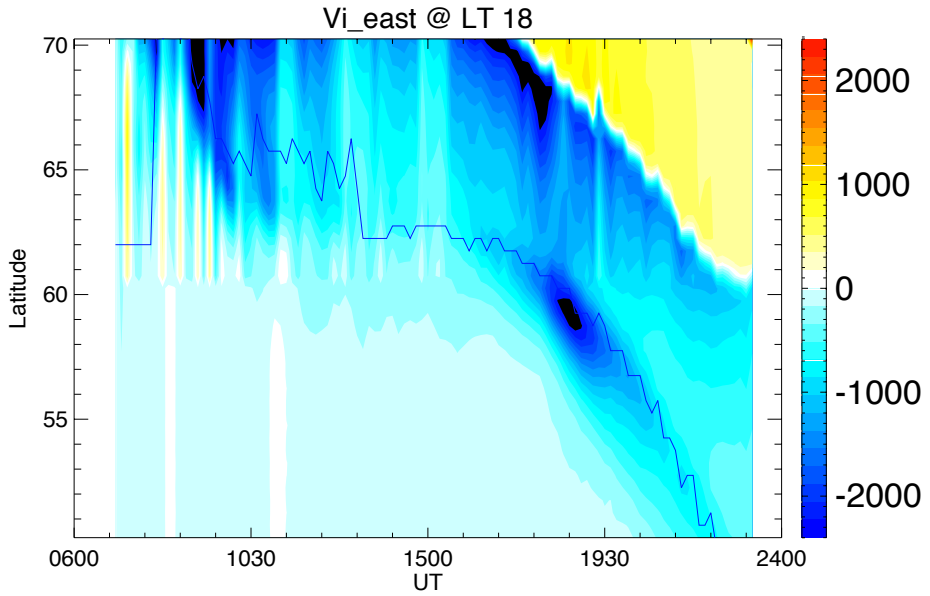

Figure 4.11 Ion drift at the 1800 LT from RCM on March 17th 2013.

Figure 4.11 shows the ion drift in the east direction at the fixed local time, 1800LT. The x-axis is the Universal Time and the y-axis represents the latitude from 50 – 70 degree. The blue line marks the location of aurora equatorward boundary. As shown in Figure 4.11, the aurora boundary moves southward when the Dst index decreased. This indicates the aurora expands when the storm is in the main phase, which is consistent to the observations. The SAPS appears around 1630 UT and reaches maximum around 1700 UT. The SAPS lasts over several hours. We know, the SAPS represents the high speed westward ion flow. Generally speaking, the ion drift is the **E** X **B** drift and highly depends on the electric field because the magnetic field at the thermosphere altitude is often considered as constant. Thus, the potential pattern contributes to the ion drift. In the RCM simulation, the potential is solved through the current continuity equation, which depends on the conductance in the ionosphere, therefore the conductance in the ionosphere is important to the SAPS formation and evolution. Some observations show that SAPS event can be co-located with the ionosphere trough phenomenon,which is the depletion of electron density and conductance in a certain localized region. Figure 4.12 below shows the Pedersen conductance from GITM simulation. Similar to the figure 4.11, we extract the simulation results at a fixed local time 1800LT and the blue line marks the aurora equatorward boundary.

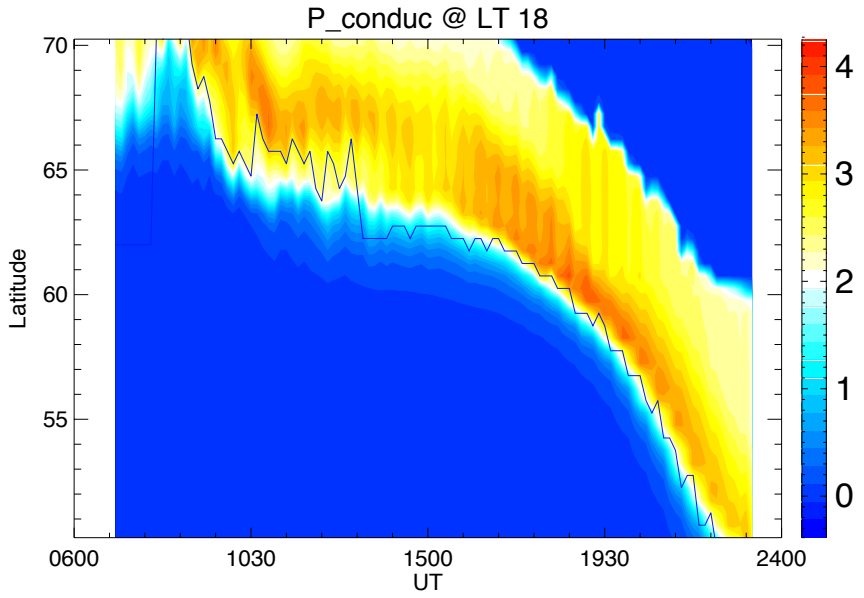

Figure 4.12 The GITM simulation results of Pedersen conductance at the 1800LT when driven by RCM outputs on March 17th 2013.

In the figure 4.12, it could be found that the conductance in the sub-aurora region does not change very much although the SAPS lasts for almost 4 hours. However, we need to point out the feedback of the ion convection does not contribute to the RCM potential solver. Therefore, we still do not include all the physics in the simulation for our 1-way coupled systems. These parts should be the future work, espically using the 2-way coupled dynamic systems.

Our simulation period for the DMSP-driven GITM is from 1650 UT to 1730 UT on March 17th 2013, but we have the observations during the whole day. We could compare the RCM-driven GITM to the DMSP observations to see how realistic the forcings GITM

received from the RCM simulation. Since the DMSP f16 is close to the 1800LT, the observations from DMSP f16 have been compared with the RCM forcing. Figure 4.13 below shows the ion drift observations in the east direction from DMSP f16. The maximum of westward ion flow at 53^0 latitude appears around 1700-1900 UT and the SAPS region is located around 52-54 degree in latitude which is lower than the RCM-driven GITM simulation. Although the small structures have some differences, the large distribution is comparable between the simulation and observation .

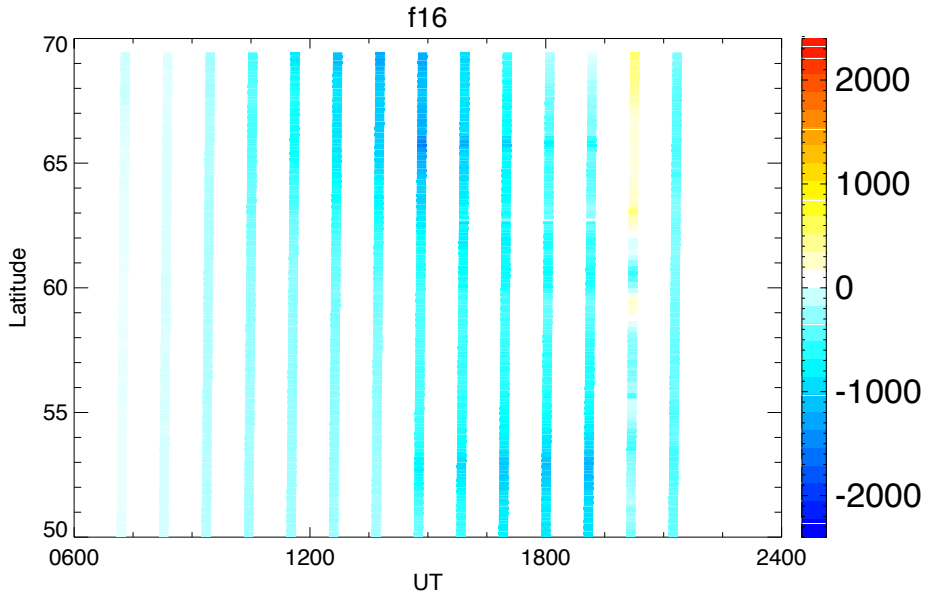

Figure 4.13 The DMSP f16 observations for ion drift on March 17th 2013.

4.5 Discussion

In this chapter, the GITM model has been used to study the St.Patrick 2013 storm event. Due to the limitation of empirical models, we used two different methods to specify the forcing to drive GITM. Both the DMSP-driven and RCM-driven methods have advantages

and disadvantages. The DMSP-driven setup is realistic in the localized region along the satellite trajectory, while RCM-driven setup provides a continuous global distribution from a physics based model. From the DMSP-driven case, we could analyze the response of neutral wind to the high-speed ion drift flow. It is found the ion drag force increased significantly in the east-west direction. The change of pressure gradient force dominates in both east-west and south-north directions. The RCM-driven case shows that the RCM forcing reproduces the SAPS phenomenon as well. The global distribution RCM provides allows us to study the formation and evolution of SAPS. Compared with the DMSP observations, RCM simulations capture the large-scale distribution of ion convection well although the localized feature has some differences. The SAPS formation is directly due to the electric field and electric potential. The potential solver in the RCM depends on the conductance of ionosphere. Definitely, the coupled system contributes to the SAPS. The formation of SAPS also indicates there are parts of energy transport to the sub-aurora region from the magnetosphere, which is one kind of important energy to the thermosphere in the lower latitude, since SAPS often generate TADS propagates to both poleward and equatorward directions.

CHAPTER 5

CONCLUSION AND FUTURE WORK

The motivation of this research is to understand the influence of energy deposition in the ionosphere at high latitudes. The high latitude region is the most dynamic region in the ionosphere and all different energy sources could have possible influence on it. To have a better understanding of the physics in the ionosphere, first, we need have a good estimation of how much external energy is deposited into the ionosphere in different kinds. Then we should estimate influence of energy deposition to the physics processes in the ionosphere. In the chapter 2 and chapter 3, we calculate the energy of Joule heating and Poynting flux from satellite observations. Chapter 4 used the observations of forcing to drive the physics based model GITM. The simulation reproduced the consequence of ionosphere disturbance to a geomagnetic storm in general.

In the chapter 2, the COSMIC electron profiles from 2009-2014 are used to calculate the Pedersen conductivity and Joule heating. The Joule heating indicates the energy dissipation from currents transportation. The results reveal that both the solar activity and geomagnetic activity can strongly influence the Pedersen conductivity. The particle precipitation influences mainly in the E region while the solar radiation influences the F region more. The Joule heating has the inter-hemispherical asymmetry and the asymmetry has strong local time dependences. The differences are larger in the post-midnight sector than in the pre-midnight sector. The results give us a good estimation of the energy distribution in different solar activities and geomagnetic activities.

In the chapter 3, the DMSP F15 SSIES data from 2000-2004 are used to calculate the Poynting flux in the polar cap boundary regions. The Poynting flux is the electromagnetic energy which indicates the energy transportation through the EM waves. The statistical results show that the average electromagnetic energy input into the LLBL region is less than that in the cusp region in general. The sensitivity of Poynting flux to the magnitude of IMF in the Y-Z plane is maximum during northward IMF conditions, the average Poynting flux is largest when By is dominant and positive. The Poynting flux and electron precipitation energy flux have a negative correlation in both cusp and LLBL region, which is more sensitive in the cusp region than in the LLBL region.

In the chapter 4, the GITM model is used to simulate the real event, St.Patrick storm in 2013. Two different ways have been used to specify the high-latitude electrodynamic forcing, from the DMSP observations and from the RCM model. The GITM results driven by those two different methods show the influence of SAPS on the sub-aurora region. It is found that the ion drag force increased significantly in the east-west direction. The pressure gradient force change is dominant in both east-west and south-north directions. RCM-driven case captures the large-scale distribution well although the localized feature shows some differences.

To better understand the ionosphere/thermosphere response to the energy deposition, more data sources are needed. More detailed model data comparisons are also need. As the data part, COSMIC II project will provide more electron density profiles in the following years. As it is shown in previous chapters, the data coverage is not good enough in the high geomagnetic activities. If more COSMIC data profile will be included,

the data coverage will be better in every category. Based on more complete data set, the cross-interaction between the solar activities and geomagnetic activities could be removed as well. This will improve the statistic results.

For the Poynting flux, more DMSP satellites will be used to calculate the Poynting flux besides F15. As discussed above, the F15 satellite has certain orbits only passing a narrow range of local time. Therefore, the results based on F15 observations in the cusp and LLBL may have a local time bias. It is not clear that if the local time bias has significant influence in the statistic results or not. The F15 particle data also have some limitation, since the high energy band data set is not reliable. If the Poynting flux could be calculated from all the DMSP F15, F16, F17, F18, the results will be more reliable.

As the model part, as we mentioned above, the RCM-driven case is for one-way coupling and RCM potential solver does not depend on the conductance calculated by GITM right now. The fully feedback mechanism is not included in the simulation. Therefore, self-consistent 2-way coupled simulation is needed to better understand the whole physics process including the SAPS feedback to the magnetosphere. Meanwhile, the simulation results should compare to observations for different cases.

References

Anthes, R. A., P. A. Berhardt, Y. Chen, L. Cucurull, K. F. Dymond, D. Ector, S. B. Healy, S. P. Ho, D. C. Hunt, and Y. H. Kuo (2008), The COSMIC/FORMOSAT-3 mission, Bull. Am. Meteorol. Soc, 89, 313–333.

Brekke, A., J. R. Doupnik, and P. M. Banks (1974), Incoherent scatter measurements of e region conductivities and currents in the auroral zone, J. Geophys. Res., 79(25), 3773–3790.

Buonsanto, M. J. (1999), Ionospheric storms—A review, Space Sci. Rev., 88, 563–601, doi:10.1023/A:1005107532631.

Burns, A. G., Z. Zeng, W. Wang, J. Lei, S. C. Solomon, A. D. Richmond, T. L. Killeen, and Y. H. Kuo (2008), Behavior of the F2 peak ionosphere over the South Pacific at dusk during quiet summer conditions from COSMIC data, J. Geophys. Res., 113, A12305, doi:10.1029/2008JA013308.

Cattell, C., J. Dombeck, and L. Hanson (2013), Solar cycle effects on parallel electric field acceleration of auroral electron beams, J. Geophys. Res. Space Physics, 118, 5673–5680, doi:10.1002/jgra.50546.

Chaston, C. C., J. W. Bonnell, C. W. Carlson, J. P. McFadden, R. E. Ergun, and R. J. Strangeway (2003), Properties of small-scale Alfvén waves and accelerated electrons from FAST, *J. Geophys. Res. Sp. Phys.*, *108*(A4), 1–16, doi:10.1029/2002JA009420.

Chen J., T.A Fritz, R.B Sheldon, H.E Spence, W.N Spjeldvik, et al. (1998), Cusp Energetic Particle Events: Implications for a Major Acceleration Region of the Magnetosphere, J. Geophys. Res., 103, 69–78.

Cheryl Yu-Ying Huang, Yanshi Huang, Yi-Jiun Su, Eric K. Sutton, Marc Rotan Hairston, William Robin Coley, Ionosphere-thermosphere (IT) response to solar wind forcing during magnetic storms (2016), Journal of Space Weather and Space Climate, 6, A4.

Cosgrove, R. B., et al. (2014), Empirical model of Poynting flux derived from FAST data and a cusp signature, J. Geophys. Res. Space Physics, 119, 411–430, doi:10.1002/2013JA019105.

Danilov, A., and J. Lastovicka (2001), Effects of geomagnetic storms on the ionosphere and atmosphere, Int. J. Geomag. Aeron., 2(3), 209–224.

Deng, Y., Fuller-Rowell, T. J., Ridley, A. J., Knipp, D., & Lopez, R. E. (2013). Theoretical study: Influence of different energy sources on the cusp neutral density enhancement. *Journal of Geophysical Research: Space Physics*, *118*(5), 2340-2349.DOI: 10.1002/jgra.50197.

Deng, Y., C. Sheng, Y.-J. Su,M. R. Hairston, D. Knipp, C. Y. Huang, D.Ober,R. J. Redmon, and R. Coley (2015), Correlation between Poyntingflux and soft electron precipitation in the dayside polar cap boundary regions, J. Geophys. Res. Space Physics, 120, doi:10.1002/2015JA021075.

Deng, Y., A. D. Richmond, A. J. Ridley and H.-L. Liu (2008), Assessment of the non-hydrostatic effect on the upper atmosphere using a general circulation model (GCM), *Geophys. Res. Lett*, 35, L01104, doi:10.1029/2007GL032182.

Deng, Y., T. J. Fuller-Rowell, A. J. Ridley, D. Knipp, and R. E. Lopez (2013), Theoretical study: Influence of different energy sources on the cusp neutral density enhancement, J. Geophys. Res. Space Physics, 118, 2340–2349, doi:10.1002/jgra.50197.

Eriksson, S., M. Maimaiti, J. B. H. Baker, K. J. Trattner, D. J. Knipp, and F. D. Wilder (2017), Dual E x B flow responses in the dayside ionosphere to a sudden IMF By rotation, Geophys. Res. Lett., 44, 6525–6533, doi:10.1002/2017GL073374.

Evans, D. S., N. C. Maynard, J. Tr.im, T. Jacobsen, and A. Egeland (1977), Auroral vector electric field and particle comparisons, Electrodynamics of an arc, J. Geophys. Res., 82(16), 2235–2249.

Fang, X., C. E. Randall, D. Lummerzheim, S. C. Solomon, M. J. Mills, D. R. Marsh, C. H. Jackman, W. Wang, and G. Lu (2008), Electron impact ionization: A new parameterization for 100 eV to 1 MeV electrons, J. Geophys. Res., 113, A09311, doi:10.1029/2008JA013384.

Fuller-Rowell, T. J., and D. S. Evans (1987), Height-integrated Pedersen and Hall conductivity patterns inferred from the TIROS-NOAA satellite data, J. Geophys. Res., 92(A7), 7606–7618.

Fuselier, S. A., J. Berchem, K. J. Trattner, and R. Friedel, Tracing ions in the cusp and low-latitude boundary layer using multispacecraft observations and a global MHD simulation, J. Geophys. Res., 107(A9), 1226, doi:10.1029/2001JA000130, 2002.

Gary, J. B., R. A. Heelis, and J. P. Thayer (1995), Summary of field-aligned poynting flux observations from DE 2, Geophys. Res. Lett., 22, 1861.

Guo, J., Y. Deng, S. Zhang (2018), The Effect of Sub-Auroral Polarization Streams on Ionosphere and Thermosphere during 2015 St. Patrick's Day storm: Global Ionosphere-Thermosphere Model Simulations,*Journal of Geophysical Research: Space Physics*, 123. https://doi.org/10.1002/2017JA024781.

Hajj, G., L. Lee, X. Pi, L. Romans, W. Schreiner, P. Straus, and C. Wang (2000), Cosmic GPS ionospheric sensing and space weather, Terr. Atmos. Oceanic Sci., 11(1), 235–272.

Hardy, D. A., M. S. Gussenhoven, R. Raistrick, and W. J. McNeil (1987), Statistical and functional representations of the pattern of auroral energy flux, number flux, and conductivity, J. Geophys. Res., 92(A11), 12,275–12,294.

He, M., L. Liu, W. Wan, B. Ning, B. Zhao, J. Wen, X. Yue, and H. Le (2009), A study of the Weddell Sea Anomaly observed by FORMOSAT-3/COSMIC, J. Geophys. Res., 114, A12309, doi:10.1029/2009JA014175.

Heikkila, W. J., and J. D. Winningham (1971), Penetration of magnetosheath plasma to low altitudes through the dayside magnetospheric cusps, J. Geophys. Res., 76(4), 883–891, doi:10.1029/JA076i004p00883.

Huang C. Y., and Burke W. J. (2004), Transient sheets of field aligned current observed by DMSP during the main phase of a magnetic superstorm, J. Geophys. Res., 109, A06303, doi:10.1029/2003JA010067.

Kaeppler, S., D. Hampton, M. Nicolls, A. Str.mme, S. Solomon, J. Hecht, and M. Conde (2015), An investigation comparing ground-based techniques that quantify auroral electron flux and conductance, J. Geophys. Res. Space Physics, 120, 9038–9056, doi:10.1002/2015JA021396.

Kelley M. C., Knudsen D. J., and Vickrey J. F. (1991), Poynting flux measurements on a satellite: A diagnostic tool for space research, J. Geophys. Res., 96, 201–207.

Kivelson, M. G., and C. T. Russell (1995), Introduction to space physics, Cambridge university press.

Kilcommons, L. M., R. J. Redmon, and D. J. Knipp (2017), A New DMSP Magnetometer & Auroral Boundary Dataset and Estimates of Field Aligned Currents in Dynamic Auroral Boundary Coordinates, J. Geophys. Res. Space Physics, 122, doi:10.1002/2016JA023342.

Knipp, D., S. Eriksson, L. Kilcommons, G. Crowley, J. Lei, M. Hairston, and K. Drake (2011), Extreme Poynting flux in the dayside thermosphere: Examples and statistics, Geophys. Res. Lett., 38, L16102, doi:10.1029/2011GL048302.

Knipp, D. J., W. K. Tobiska, and B. A. Emery (2004), Direct and indirect thermospheric heating sources for solar cycles 21–23, Sol. Phys., 224, 495–505, doi:10.1007/s11207-005-6393-4.

Laundal, K. M., and N. .stgaard (2009), Asymmetric auroral intensities in the Earth's Northern and Southern Hemispheres, Nature, 460(7254), 491–493.

Le, G., J. Slavin, and R. Strangeway (2010), Space Technology 5 observations of the imbalance of regions 1 and 2 field-aligned currents and its implication to the cross-polar

cap Pedersen currents, Journal of Geophysical Research: Space Physics (1978–2012), 115 (A7).

Lei, J., S. Syndergaard, A. G. Burns, S. C. Solomon, W. Wang, Z. Zeng, R. G. Roble, Q. Wu, Y. H. Kuo, and J. M. Holt (2007), Comparison of COSMIC ionospheric measurements with ground-based observations and model predictions: Preliminary results, J. Geophys. Res., 112, A07308, doi:10.1029/2006JA012240.

Li, W., D. Knipp, J. Lei, and J. Raeder (2011), The relation between dayside local Poynting flux enhancement and cusp reconnection, J. Geophys. Res., 116, A08301, doi:10.1029/2011JA016566.

Lutz Rastätter, Ja Soon Shim, Maria M. Kuznetsova, Liam M. Kilcommons, Delores J. Knipp, Mihail Codrescu, Tim Fuller-Rowell, Barbara Emery,Daniel R. Weimer, Russell Cosgrove, Michael Wiltberger, Joachim Raeder,Wenhui Li, Gábor Tóth, Daniel Welling, GEM-CEDAR challenge: Poynting flux at DMSP and modeled Joule heat (2016), Space Weather, 14, 2, 113

Lu, G., et al. (1994), Interhemispheric asymmetry of the high-latitude ionospheric convection pattern, J. Geophys. Res., 99(A4), 6491–6510.

Luan, X., W. Wang, A. Burns, S. C. Solomon, and J. Lei (2008), Midlatitude nighttime enhancement in F region electron density from global COSMIC measurements under solar minimum winter condition, J. Geophys. Res., 113, A09319, doi:10.1029/2008JA013063.

Luan, X., W. Wang, A. Burns, S. Solomon, Y. Zhang, and L. J. Paxton (2010), Seasonal and hemispheric variations of the total auroral precipitation energy flux from TIMED/GUVI, J. Geophys. Res., 115, A11304, doi:10.1029/2009JA015063.

Lukianova, R., C. Hanuise, and F. Christiansen (2008), Asymmetric distribution of the ionospheric electric potential in the opposite hemispheres as inferred from the SuperDARN observations and FAC-based convection model, J. Atmos. Sol. Terr. Phys., 70(18), 2324–2335.

Lu Y., Y. Deng, C. Sheng, L. Kilcommons, D. Knipp (2018), Poynting Flux in the Dayside Polar Cap Boundary Regions from DMSP F15 satellite measurements, *J. Geophys. Res*., 123. https://doi.org/10.1002/2018JA025309.

McGranaghan, R., D. J. Knipp, T. Matsuo, H. Godinez, R. J. Redmon, S. C. Solomon, and S. K. Morley (2015), Modes of high-latitude auroral conductance variability derived from DMSP energetic electron precipitation observations: Empirical orthogonal function analysis,J. Geophys. Res. Space Physics, 120, 11,013–11,031, doi:10.1002/2015JA021828.

McGranaghan, R., D. J. Knipp, T.Matsuo, and E. Cousins (2016), Optimal interpolation analysis of high-latitude ionospheric Hall and Pedersen conductivities: Application to assimilative ionospheric electrodynamics reconstruction, J. Geophys. Res. Space Physics, 121, 4898–4923, doi:10.1002/2016JA022486.

McHarg, M., F. Chun, D. Knipp, G. Lu, B. Emery, and A. Ridley (2005), High-latitude Joule heating response to IMF inputs, J. Geophys. Res., 110, A08309, doi:10.1029/2004JA010949.

Mende, S. B., H. U. Frey, and V. Angelopoulos (2016), Source of the dayside cusp aurora, J. Geophys. Res. Space Physics, 121, 7728–7738,doi:10.1002/2016JA022657.

Millward, G. H., R. J. Moffett, H. F. Balmforth, and A. S. Rodger (1999), Modeling the ionospheric effects of ion and electron precipitation in the cusp, J. Geophys. Res., 104, 24,603–24,612, doi:10.1029/1999JA900249.

Moen, J., and A. Brekke (1990), On the importance of ion composition to conductivities in the auroral ionosphere, J. Geophys. Res., 95, 10,687–10,693, doi:10.1029/JA095iA07p10687.

Moen, J., and A. Brekke (1993), The solar flux influence on quiet time conductances in the auroral ionosphere, Geophys. Res. Lett., 20(10),971–974.

Moldwin, M. (2008), An Introduction to Space Weather, Cambridge Univ. Press, Cambridge, U. K.

Newell, P. T. and Meng, C. I.: The cusp and the cleft/LLBL: Low altitude identification and statistical local time variation (1988), J. Geophys. Res, 93, No. A12, 14 549–14 556, 1988.

Newell, P. T., Meng, C. I., Sibeck, D. G., and Lepping, P.: Some low-altitude cusp dependencies on the interplanetary magnetic field (1989), J. Geophys. Res, 94, No. A7, 8921–8927.

Newell, P. T., K. Liou, and G. R. Wilson (2009), Polar cap particle precipi- tation and aurora: Review and commentary, J. Atmos. Sol-Terr. Phys., 71, 199–215, doi:10.1016/j.jastp.2008.11.004.

Newell, P. T., C.-I. Meng, and S. Wing (1998), Relation to solar activity of intense aurorae in sunlight and darkness, Nature, 393(6683),342–344.

Newell, P. T., T. Sotirelis, and S. Wing (2009), Diffuse, monoenergetic, and broadband aurora: The global precipitation budget, J. Geophys. Res., 114, A09207, doi:10.1029/2009JA014326.

Pedatella, N. M., H.-L. Liu, F. Sassi, J. Lei, J. L. Chau, and X. Zhang (2014), Ionosphere variability during the 2009 SSW: Influence of the lunar semidiurnal tide and mechanisms producing electron density variability, J. Geophys. Res. Space Physics, 119, 3828–3843, doi:10.1002/2014JA019849.

Pedatella, N. M., X. Yue, and W. S. Schreiner (2015), An improved inversion for FORMOSAT-3/COSMIC ionosphere electron density profiles, J. Geophys. Res. Space Physics, 120, 8942–8953, doi:10.1002/2015JA021704.

Pettigrew, E., S. Shepherd, and J. Ruohoniemi (2010), Climatological patterns of high-latitude convection in the Northern and Southern Hemispheres: Dipole tilt dependencies and interhemispheric comparisons, J. Geophys. Res., 115, A07305, doi:10.1029/2009JA014956.

Potemra, T. A., W. K. Peterson, J. P. Doering, C. O. Bostrom, R. W. McEntire, and R. A. Hoffman (1977), Low-energy particle observations in the quiet dayside cusp from AE-C and AE-D, J. Geophys. Res., 82(29), 4765–4776, doi:10.1029/JA082i029p04765.

Prölss, G. W. (2006), Electron temperature enhancement beneath the magnetospheric cusp, J. Geophys. Res., 111, A07304, doi:10.1029/2006JA011618.

Provan, G. T. K. Yeoman, S. W. H. Cowley (1999), The influence of the IMF B_y component on the location of pulsed flows in the dayside ionosphere observed by an HF radar, Geophys. Res. Lett, 26, 521-524, DOI: 10.1029/1999GL900009

Rasmussen, C. E., R. W. Schunk, and V. B. Wickwar (1988), A photochemical equilibrium model for ionospheric conductivity, J. Geophys. Res., 93(A9), 9831–9840.

Richmond, A. D., and G. Lu (2000), Upper-atmospheric effects of magnetic storms: A brief tutorial, J. Atmos. Sol. Terr. Phys., 62, 1115–1127, doi:10.1016/S1364 6826(00)00094-8.

Rastätter, L., J. S. Shim, M. M. Kuznetsova, L. M. Kilcommons, D. J. Knipp, M. Codrescu, T. Fuller-Rowell, B. Emery, D. R. Weimer, R. Cosgrove, et al. (2016), GEM-CEDAR challenge: Poynting flux at DMSP and modeled Joule heat, Space Weather, 14, 113–135, doi:10.1002/2015SW001238.

Redmon, R. J., W. F. Denig, L. M. Kilcommons, and D. J. Knipp (2017), New DMSP database of precipitating auroral electrons and ions, J. Geophys. Res. Space Physics,122, doi:10.1002/2016JA023339.

Ridley, A., Deng, Y., and Toth, G. (2006), The global Ionosphere-Thermosphere model, *J. Atmos. Solar-Terr. Phys.*, 68, 839-864.

Ridley, A. J., D. Zhang, and Z. Xiao (2012), Analyzing the hemispheric asymmetry in the thermospheric density response to geomagnetic storms, J. Geophys. Res., 117, A08317, doi:10.1029/2011JA017259.

Rich, F. J., D. D. Hardy, and M. S. Gussenhoven (1985), Enhanced ionosphere-magnetosphere data from the DMSP satellites, Eos Trans. AGU, 66(26), 513–514, doi:10.1029/EO066i026p00513.

Rich, F. J., and M. Hairston (1994), Large-scale convection patterns observed by DMSP, J. Geophys. Res., 99(A3), 3827–3844, doi:10.1029/93JA03296.

Richmond, A. D. (2010), On the ionospheric application of Poynting's theorem, J. Geophys. Res., 115, A10311, doi:10.1029/2010JA015768.

Robinson, R. M., and R. R. Vondrak (1984), Measurements of E region ionization and conductivity produced by solar illumination at high latitudes, J. Geophys. Res., 89(A6), 3951–3956.

Robinson, R. M., R. R. Vondrak, K. Miller, T. Dabbs, and D. Hardy (1987), On calculating ionospheric conductances from the flux and energy of precipitating electrons, J. Geophys. Res., 92, 2565–2569, doi:10.1029/JA092iA03p02565.

Rocken, C., K. Ying-Hwa, W. S. Schreiner, D. Hunt, S. Sokolovskiy, and C. McCormick (2000), COSMIC system description, Terr. Atmos. Oceanic Sci., 11(1), 21–52.

Scherer, K., H. Fichtner, B. Heber, and U. Mall (2005), Space Weather: The Physics Behind a Slogan, Springer, Berlin.

Russell, C. T., Le, G. and Petrinec, S. M.: Cusp observations of high and low latitude reconnection under northward IMF: and alternate view (2000), J. Geophys. Res., 105, No. A3, 5489–5495.

Schreiner, W., C. Rocken, S. Sokolovskiy, S. Syndergaard, and D. Hunt (2007), Estimates of the precision of GPS radio occultations from the COSMIC/FORMOSAT-3 mission, Geophys. Res. Lett., 34, L04808, doi:10.1029/2006GL027557.

Sheng, C., Y. Deng, X. Yue, and Y. Huang (2014), Height-integrated Pedersen conductivity in both E and F regions from COSMIC observations, J. Atmos. Sol. Terr. Phys., 115, 79–86, doi:10.1016/j.jastp.2013.12.013.

Spiro, R. W., P. H. Reiff, and L. J. Maher Jr. (1982), Precipitating electron energy flux and auroral zone conductances—An empirical model, J. Geophys. Res., 87, 8215–8227, doi:10.1029/JA087iA10p08215.

Strangeway, R. J. (2012), The equivalence of Joule dissipation and frictional heating in the collisional ionosphere, J. Geophys. Res., 117, A02310, doi:10.1029/2011JA017302.

Thayer, J. P., J. F. Vickrey, R. A. Heelis, and J. B. Gary (1995), Interpretation and modeling of the high-latitude electromagnetic energy flux, J. Geophys. Res., 100(A10), 19,715–19,728.

Sandholt, P. E. , J. Moen and D. Opsvik, Periodic auroral events at the midday polar cap boundary: implications for solar wind magnetosphere coupling , Geophys. Res. Lett, 19, 1223, 1992, DOI: 10.1029/92GL01275

Sandholt, P. E., and C. J. Farrugia (2007), Role of poleward moving auroral forms in the dawn-dusk auroral precipitation asymmetries induced by IMF By, J. Geophys. Res., 112, A04203, doi:10.1029/2006JA011952.

Saunders, M. A., (1989) Origin of the cusp Birkeland current, Geophys. Res. Lett., 16, 151, doi:10.1029/GL016i002p00151

Savin, S. P., et al. (1998), Interball tail probe measurements in outer cusp and boundary layers, in Geospace Mass and Energy Flow: Results from the International Solar-Terrestrial Physics Program, Geophys. Monogr. Ser., vol. 104, edited by J. L. Horwitz, D. L. Gallagher, and W. K. Peterson, pp. 25 – 44, AGU, Washington, D. C.

Schunk, R., and A. Nagy (2009), Ionospheres: physics, plasma physics, and chemistry, Cambridge university press.

Sheng C, Deng Y, Wu Q, et al. Thermospheric winds around the cusp region (2015), J. Geophys. Res., 120(2): 1248-1255, doi: 10.1002/2014JA020028.

Sheng, C., Y. Deng, Y. Lu, X. Yue (2017), Dependence of Pedersen conductance in the E and F regions and their ratio on the solar and geomagnetic activities, *Space Weather*, doi:10.1002/2016SW001486.

Smith, M. F., and M. Lockwood (1996), Earth's magnetospheric cusps, Rev. Geophys., 34(2), 233–260, doi:10.1029/96RG00893.

Strangeway, R. J., C. T. Russell, C. W. Carlson, J. P. McFadden, R. E. Ergun, M. Temerin, D. M. Klumpar, W. K. Peterson, and T. E. Moore (2000), Cusp field-aligned currents and ion outflows, J. Geophys. Res., 105, 21,129–21,142.

Strangeway, R. J., R. E. Ergun, Y.-J. Su, C. W. Carlson, and R. C. Elphic (2005), Factors controlling ionospheric outflows as observed at intermediate altitudes, J. Geophys. Res., 110, A03221, doi:10.1029/2004JA010829.

Trattner, K. J., S. M. Petrinec, S. A. Fuselier, and T. D. Phan (2012), The location of reconnection at the magnetopause: Testing the maximum magnetic shear model with THEMIS observations, J. Geophys. Res., 117, A01201, doi:10.1029/2011JA016959.

Tsyganenko, N. A. (1995), Modeling the Earth's magnetospheric magnetic field confined within a realistic magnetopause, J. Geophys. Res., 100(A4), 5599–5612, doi:10.1029/94JA03193.

Vickrey, J. F., R. R. Vondrak, and S. J. Matthews (1981), The diurnal and latitudinal variation of auroral zone ionospheric conductivity, 86(A1), 65–75, doi:10.1029/JA086iA01p00065.

Wu, B. H., V. Chu, P. Chen, and T. Ting (2005), FORMOSAT-3/COSMIC science mission update, GPS Solutions, 9(2), 111–121.

Xing, Z. Y.; Yang, H. G.; Han, D. S.; Wu, Z. S.; Hu, Z. J.; Zhang, Q. H.; Kamide, Y.; Hu, H. Q.; Zhang, B. C.; Liu, J. M.; Huang, D. H.. (2012) *Poleward moving auroral forms* (*PMAFs*) *observed* at the *Yellow River Station*: A *statistical study* of *its dependence* on the *solar wind conditions*, Journal of Atmospheric and Solar-Terrestrial Physics, 86: 25-33, https://doi.org/10.1016/j.jastp.2012.06.004

Yordanova, E., Sundkvist, D., Buchert, S. C., et al. (2007), Energy input from the exterior cusp into the ionosphere: Correlated ground-based and satellite observations Geophys. Res. Lett., 34, L04102

Yue, X., W. S. Schreiner, J. Lei, C. Rocken, Y. H. Kuo, and W. Wan (2010a), Climatology of ionospheric upper transition height derived from COSMIC satellites during the solar minimum of 2008, J. Atmos. Sol. Terr. Phys., 72(17), 1270–1274.

Yue, X., W. S. Schreiner, J. Lei, C. Rocken, D. C. Hunt, Y. H. Kuo, and W. Wan (2010b), Global ionospheric response observed by COSMIC satellites during the January 2009 stratospheric sudden warming event, J. Geophys. Res., 115, A00G09, doi:10.1029/2010JA015466.

Yue, X., W. S. Schreiner, C. Rocken, Y. H. Kuo, and J. Lei (2012), Artificial ionospheric wave number 4 structure below the F2 region due to the Abel retrieval of radio occultation measurements, GPS Solutions, 16, 1–7.

Yue, X., W. S. Schreiner, Y.-H. Kuo, Q. Wu, Y. Deng, and W. Wang (2013), GNSS radio occultation (RO) derived electron density quality in high latitude and polar region: NCAR-TIEGCM simulation and real data evaluation, J. Atmos. Sol. Terr. Phys., 98, 39–49, doi:10.1016/j.jastp.2013.03.009.

Zeng, Z., A. Burns, W. Wang, J. Lei, S. Solomon, S. Syndergaard, L. Qian, and Y.-H. Kuo (2008), Ionospheric annual asymmetry observed by the COSMIC radio occultation measurements and simulated by the TIEGCM, J. Geophys. Res., 113, A07305, doi:10.1029/2007JA012897.

Zhang, B., W. Lotko, O. Brambles, M. Wiltberger, W. Wang, P. Schmitt, and J. Lyon (2012), Enhancement of thermospheric mass density by soft electron precipitation, Geophys. Res. Lett., 39, L20102, doi:10.1029/2012GL053519.

Zheng, L., S. Fu, Q. Zong, G. Parks, C. Wang, and X. Chen (2013), Solar cycle dependence of the seasonal variation of auroral hemispheric power, Chin. Sci. Bull., 58(4–5), 525–530.

Zhou, S., X. Luan, and X. Dou (2016), Solar activity dependence of nightside aurora in winter conditions, J. Geophys. Res. Space Physics, 121,1619–1626, doi:10.1002/2015JA021865.

Z̆ivković, T., Buchert, S., Ritter, P., Palin, L., & Opgenoorth, H. (2015), Investigation of energy transport and thermospheric upwelling during quiet magnetospheric and ionospheric conditions from the studies of low- and middle-altitude cusp Annales Geophysicae, 33, 623